A fusion model integrating magnetic resonance imaging radiomics and deep learning features for predicting alpha-thalassemia X-linked intellectual disability mutation status in isocitrate dehydrogenase–mutant high-grade astrocytoma: a multicenter study

Zhi Liu[1#], Xinyi Xu[2#], Wang Zhang[3#], Liqiang Zhang[2], Ming Wen[2], Jueni Gao[2], Jun Yang[4], Yubo Kan[5], Xing Yang[6], Zhipeng Wen[7], Shanxiong Chen[3], Xu Cao[5]

[1]Department of Radiology, Chongqing Hospital of Traditional Chinese Medicine, Chongqing, China; [2]Department of Radiology, The First Affiliated Hospital of Chongqing Medical University, Chongqing, China; [3]College of Computer & Information Science, Southwest University, Chongqing, China; [4]Department of Endocrinology, University-Town Hospital of Chongqing Medical University, Chongqing, China; [5]School of Medical and Life Sciences Chengdu University of Traditional Chinese Medicine, Chengdu, China; [6]Department of Radiology, Chongqing United Medical Imaging Center, Chongqing, China; [7]Department of Radiology, Sichuan Cancer Hospital & Institute, Sichuan Cancer Center, School of Medicine, University of Electronic Science and Technology of China, Chengdu, China

Contributions: (I) Conception and design: Z Liu, X Xu, S Chen, X Cao; (II) Administrative support: M Wen; (III) Provision of study materials or patients: J Gao, X Yang, Z Wen; (IV) Collection and assembly of data: L Zhang, J Yang, Y Kan; (V) Data analysis and interpretation: W Zhang, S Chen; (VI) Manuscript writing: All authors; (VII) Final approval of manuscript: All authors.

#These authors contributed equally to this work.

Correspondence to: Zhipeng Wen, MD. Department of Radiology, Sichuan Clinical Research Center for Cancer, Sichuan Cancer Hospital & Institute, Sichuan Cancer Center, Affiliated Cancer Hospital of University of Electronic Science and Technology of China, No. 55, Section 4, Renmin South Road, Chengdu 610042, China. Email: 18080876075@163.com; Shanxiong Chen, PhD. College of Computer & Information Science, Southwest University, No. 2 Tiansheng Road, Beibei District, Chongqing 400715, China. Email: csxpml@163.com; Xu Cao, MD. School of Medical and Life Sciences Chengdu University of Traditional Chinese Medicine, No. 37, 12 Qiao Road, Chengdu 610032, China. Email: 304854423@qq.com.

Background: The mutational status of alpha-thalassemia X-linked intellectual disability (*ATRX*) is an important indicator for the treatment and prognosis of high-grade gliomas, but reliable *ATRX* testing currently requires invasive procedures. The objective of this study was to develop a clinical trait-imaging fusion model that combines preoperative magnetic resonance imaging (MRI) radiomics and deep learning (DL) features with clinical variables to predict *ATRX* status in isocitrate dehydrogenase (*IDH*)-mutant high-grade astrocytoma.

Methods: A total of 234 patients with *IDH*-mutant high-grade astrocytoma (120 *ATRX* mutant type, 114 *ATRX* wild type) from 3 centers were retrospectively analyzed. Radiomics and DL features from different regions (edema, tumor, and the overall lesion) were extracted to construct multiple imaging models by combining different features in different regions for predicting *ATRX* status. An optimal imaging model was then selected, and its features and linear coefficients were used to calculate an imaging score. Finally, a fusion model was developed by combining the imaging score and clinical variables. The performance and application value of the fusion model were evaluated through the comparison of receiver operating characteristic curves, the construction of a nomogram, calibration curves, decision curves, and clinical application curves.

Results: The overall hybrid model constructed with radiomics and DL features from the overall lesion was

identified as the optimal imaging model. The fusion model showed the best prediction performance with an area under curve of 0.969 in the training set, 0.956 in the validation set, and 0.949 in the test set as compared to the optimal imaging model (0.966, 0.916, and 0.936, respectively) and clinical model (0.677, 0.641, 0.772, respectively).

Conclusions: The clinical trait-imaging fusion model based on preoperative MRI could effectively predict the *ATRX* mutation status of individuals with *IDH*-mutant high-grade astrocytoma and has the potential to help patients through the development of a more effective treatment strategy before treatment.

Keywords: Radiomics; deep learning (DL); magnetic resonance imaging (MRI); brain neoplasms; astrocytoma

Introduction

Gliomas are common primary malignant tumors in the brain and can be categorized into different subtypes based on their histopathological characteristics (1). The presence of the same genetic alterations in patients with different pathological histological classifications of glioma suggests that they may have similar biological behavior and prognosis (2). Therefore, isocitrate dehydrogenase (*IDH*)–mutant astrocytoma is classified as a distinct type in the 2021 World Health Organization (WHO) Central Nervous System (CNS) Tumor Classification Criteria. It is classified into 3 grades, WHO CNS grades 2 to 4, based on histological morphology and features (3,4). High-grade glioma (grades 3 and 4) involves a poor prognosis and a low cure rate due to the lack of effective treatments (1). However, patients with glioblastoma with alpha-thalassemia X-linked intellectual disability (*ATRX*) deletion experience a longer overall survival time and benefit more from temozolomide (TMZ) treatment (5). The combination therapy of TMZ and multitargeted receptor tyrosine kinase inhibitors (RTKis) may expand the therapeutic window for patients with high-grade gliomas carrying *ATRX* mutations (1). There are significant differences in the treatment approach and prognosis between high- and low-grade *IDH*-mutant astrocytoma (6). Therefore, knowledge of the mutational status of *ATRX* is important for both the prognostic assessment and treatment options in high-grade *IDH*-mutant astrocytoma.

The most common methods for detecting *ATRX* mutation status are based on sequencing or immunohistochemistry after biopsy or surgical excision (7,8). However, brain biopsy is often hampered by factors such as the patient's poor health condition and tumor location or patient's refusal to undergo invasive tests. Additionally, the accuracy of gene detection can be compromised by limited tissue samples, and biopsies involve certain risks, such as brain swelling, bleeding, and other neurological issues (9). Therefore, noninvasively predicting the *ATRX* mutation status of *IDH*-mutant high-grade astrocytoma could have considerable clinical value.

Imaging techniques have the advantage over standard pathological examination of being able to analyze the invasive, non-resected components of gliomas and thus capture and characterize the status of the tumor as a whole. To facilitate a consistent and standardized analysis of qualitative magnetic resonance imaging (MRI) features, the Visually Accessible Rembrandt Images (VASARI) terminology was developed (10). Previous studies have shown that VASARI features are biologically relevant to glioblastoma (11). Radiomics can extract high-throughput quantitative features that reveal tumor information from MRI images, and mathematical models based on these quantitative features can predict tumor phenotypes (12). As a common type of artificial neural network in deep learning (DL), convolutional neural networks (CNNs) have been proven capable of performing well in both image recognition and segmentation (13,14). DL and radiomics based on conventional and functional MRI have been widely used for preoperative differential diagnosis, grading, genotyping, and prognosis of gliomas (15-17). They have demonstrated good performance in predicting O6-methylguanine-DNA methyltransferase (*MGMT*) promoter methylation and *IDH* mutation in diffuse glioma (18,19). A radiomics approach based on multiparametric MRI can noninvasively determine the molecular status of *IDH1* and *ATRX* in patients with low-grade glioma (LGG) (20). In a previous study (21), a clinical radiomics–
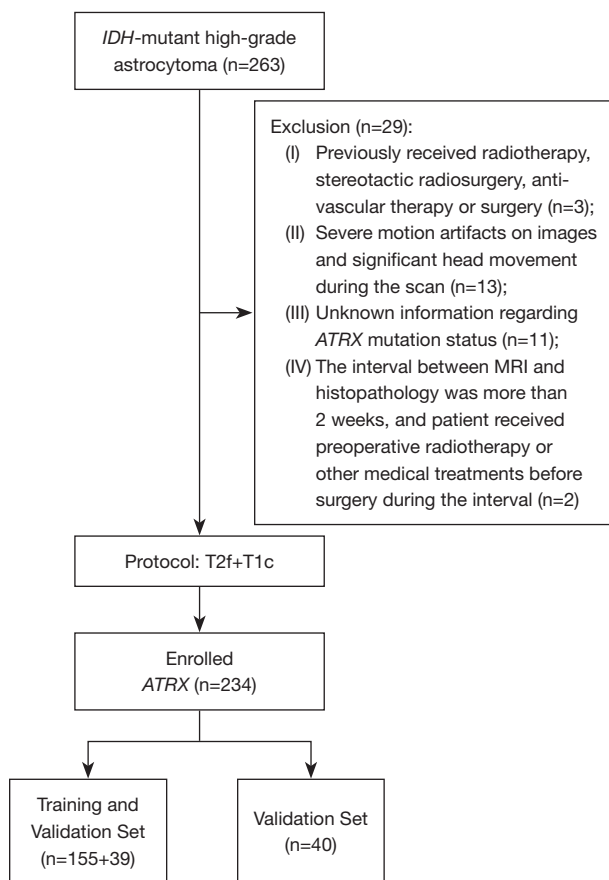
Figure 1 The patient screening process. ATRX, alpha-thalassemia X-linked intellectual disability; T2f, T2 fluid-attenuated inversion recovery; T1c, contrast-enhanced T1-weighted; IDH, isocitrate dehydrogenase; MRI, magnetic resonance imaging.

integrated model based on ^{18}F-fluorodeoxyglucose positron emission tomography (^{18}F-FDG PET) and multimodal MRI successfully predicted the *ATRX* mutation status of patients with *IDH*-mutant LGG. Although the findings of these studies are promising, the primary focus has been on LGG, and the noninvasive prediction of *ATRX* mutational status in high-grade *IDH*-mutant astrocytoma has not yet been examined. Since functional MRI and PET imaging are not as widely available as is conventional MRI (cMRI), it is necessary to thoroughly investigate the potential of cMRI in predicting *ATRX* mutation status in patients with *IDH*-mutant high-grade astrocytoma.

In this study, we aimed to combine the quantitative and qualitative features derived from cMRI and clinical variables to build a fusion model to predict *ATRX* mutation status in *IDH*-mutant high-grade astrocytoma. We present

this article in accordance with the TRIPOD reporting checklist (available at https://qims.amegroups.com/article/view/10.21037/qims-23-807/rc).

Methods

Patients

From January 2017 to June 2022, this study analyzed data from 3 different institutions: the First Affiliated Hospital of Chongqing Medical University, Sichuan Cancer Hospital, and Chongqing United Medical Imaging Center. The data and pathological information were obtained from a total of 234 patients with *IDH*-mutant astrocytoma classified as WHO CNS grades 3 or 4 according to the 2021 WHO criteria. Of these patients, 120 had *ATRX* mutations.

This study was conducted in accordance with the Declaration of Helsinki (as revised in 2013) and was approved by the institutional review boards of Chongqing Medical University, Sichuan Cancer Hospital, and the United Medical Imaging Center. All participating institutions were formally informed and agreed to the protocol of the study. Given the retrospective nature of the design, the requirements for informed consent from patients was waived. The inclusion criteria were patients with pathologically confirmed astrocytoma, *IDH*-mutant status, WHO CNS grades 3 or 4, available MRI with conventional sequences including T2 fluid-attenuated inversion recovery (T2f) and contrast-enhanced T1-weighted (T1c) images, available information regarding *ATRX* mutation status, and available clinical features including gender and age. The exclusion criteria included images with severe artifacts; previous treatment with radiotherapy, stereotactic radiosurgery, anti-vascular therapy, or surgery; and unknown *ATRX* mutation status. The patient screening process is shown in *Figure 1*.

Detection of ATRX

The tumor samples were preserved in a 10% formaldehyde solution at room temperature for a full day, encased in paraffin, and then sliced into sections 3.5-μm thick. The primary antibodies were applied for immunohistochemistry following the guidelines provided by the manufacturer (Cell Signaling Technology, Boston, USA). Each tissue section was treated with a 3% hydrogen peroxide solution at 37 ℃ for 10 min, which was followed by an overnight incubation with the primary antibody at 4 ℃. Finally, sections were exposed to goat anti-mouse/rabbit immunoglobin G (IgG)

antibodies for half an hour at room temperature using a 1:100 dilution. The staining with the DAB Detection Kit (ZSGB-BIO, Beijing, China) was observed using a Nikon microscope (Nikon Corporation, Tokyo, Japan; magnification 40×).

Assessment of qualitative clinical variables

The VASARI feature set consists of 30 categorical variables, such as tumor location, proportion enhancing, and proportion of edema (additional details about the VASARI scoring standard can be found in Table S1). The VASARI features were assessed by 2 radiologists with 5- and 10-year experience, respectively, under a double-blind method, and any disagreements were resolved by a neuroradiologist with 15-year experience. For each case, a VASARI score was constructed from the VASARI feature set and considered as a clinical variable along with age, gender, and WHO grading, to differentiate it from the imaging score calculated based on radiomics features, which is described in a later section.

Image preprocessing and region of interest (ROI) segmentation

MR images, including T1c and T2f, were acquired from various 3.0T MRI scanners using different acquisition parameters. The specific acquisition protocols can be found in Table S2. To minimize differences in imaging parameters across devices, all images underwent preprocessing steps such as registration, bias correction, intensity normalization, and resampling. Additional information regarding the image preprocessing can be found in Appendix 1 (22,23).

The segmentation of the 3-dimensional ROI was performed by 2 radiologists with 5 and 10 years of experience, respectively, using 3D-slicer software (version 4.3; https://www.slicer.org) (24). They manually segmented the ROIs of the overall lesion (enhancing tumor + edema) and enhancing tumor area from T2f and T1C, respectively, to obtain the ROI of edema habitat determination (25). If the difference between the ROIs obtained by the 2 radiologists was less than 5%, the final ROI was determined as the overlapping region of the 2 ROIs. Otherwise, it was determined by the neuroradiologist with 15 years of experience. None of these 3 experts knew of the final diagnosis or *ATRX* mutation status. The overall process of the experiment after image preprocessing is shown in *Figure 2*.

Feature extraction

The extraction of radiomics features was performed using the open-source software Pyradiomics (version 3.0.1; https://www.radiomics.io/index.html). The radiomics features derived from the ROI of edema habitat (edema), enhancing tumor (tumor), and overall lesion (overall) were extracted in both T1c and T2f images. A total of 1111 radiomics features were extracted for each ROI. For more information regarding these features, please refer to Appendix 1.

Deep features were extracted from pretrained residual network 34 (ResNet34) using transfer learning. The Pytorch (version 1.9.0; https://pytorch.org) framework was used for CNN network construction and feature extraction. The CNN network uses the well-known ResNet34, which inputs a 224×224×3 pixels natural image, and after multiple consecutive convolutional layers and pooling layers, it can output a 1,000-dimensional vector, which we regarded as the depth feature extracted from the image. Weights were pretrained using the open-source dataset ImageNet-1k (https://www.image-net.org/download.php). The slices with the largest edema area and tumor area were selected from T1c and T2f sequences, and then the ROI region was cut out. Following this, the image was enlarged to 224×224 using the bilinear interpolation algorithm, which was copied into 3 channels for input into the ResNet34. After inputting the ROI image were input into the model, a 1,000-dimensional depth feature was extracted from each ROI region of each sequence. Deep features and radiomics features were combined for subsequent filtering.

Feature selection

The feature data extracted from different ROIs were standardized with z scores. To improve the generalization performance of the model, the independent samples t-test was first used for the preliminary filtering of features, significant features were selected ($P<0.05$), the least absolute shrinkage and selection operator (LASSO) was applied for further dimension reduction, and the area under curve (AUC) was used as the evaluation index. The optimal parameter λ was determined through 10-fold cross-validation, and features with a nonzero coefficient were selected. If there were still many features after LASSO filtering (according to rule of thumb, the sample size needs to cover 10–15 observations per predictor variable to yield a stable estimate; in our study, the sample size was 194, so we aimed to keep the number of features below 20), the Akaike
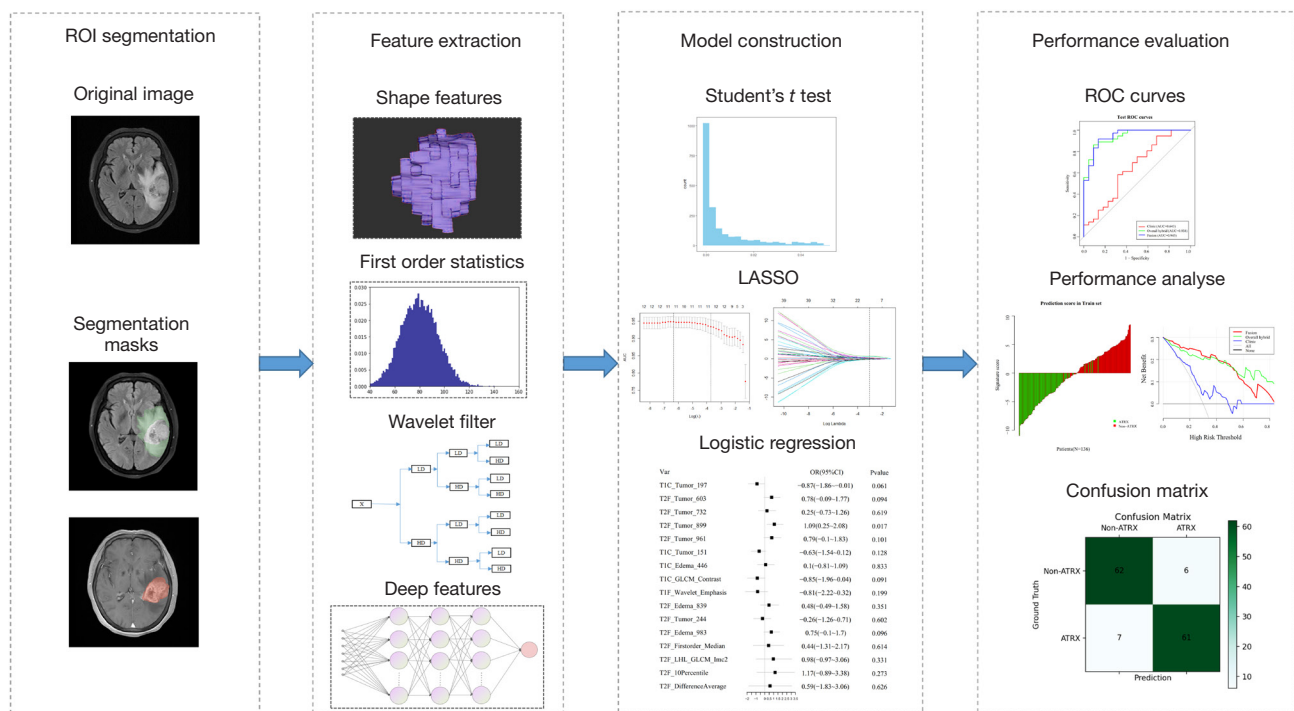
Figure 2 The workflow of the experiment divided into 4 steps: ROI segmentation, feature extraction, model construction, and performance evaluation. LASSO, least absolute shrinkage and selection operator; ROC, receiver operating characteristic; LD, low-pass digital filter; HD, high-pass digital filter; ATRX, alpha-thalassemia X-linked intellectual disability; ROI, region of interest.

information criterion (AIC) was used as the evaluation index, and the optimal feature subset was obtained using the backward step search algorithm.

Imaging model building and signature building

We utilized filtered features to construct logistic regression (LR), random forest (RF), and support vector machine (SVM) models. LR was chosen as the classifier for subsequent model building due to its superior generalization performance. Based on the combination of 3 types of features (radiomics, DL, and radiomics + DL as the hybrid feature) in different regions, 9 imaging models were constructed to verify the prediction effect of different types of features and ROI regions on *ATRX* mutation status, and the image models were named according to the combination of feature types (i.e., radiomics, DL, hybrid) and feature source (i.e., edema, tumor, overall). The optimal imaging model was selected according to the average AUC of the models with 5-fold cross-validation.

Based on the optimal imaging model, an imaging signature was constructed using a linear combination of coefficients weighted features (i.e., first feature coefficient × first feature value + … + nth feature coefficient × nth feature value). The imaging score for each patient was then calculated. The formula for calculating the imaging score of imaging features can be found in Appendix 2, and patients were divided into high-risk group and low-risk group according to a cutoff value of 0.48.

Clinical model building

Clinical variables included age, sex, WHO grade, and VASARI score. More detailed information on the clinical variables can be found in Table S3. A multivariate logical regression model was constructed using clinical variables.

Fusion model building and performance evaluation

A fusion predictive model was constructed by combining clinical variables and image scores obtained from the optimal imaging model. To assess the performance and utility of the fusion model, several methods were employed, including receiver operating characteristic (ROC) analysis,

Table 1 The clinical characteristics of patients in 3 centers

Clinical characteristics	Cohort A (N=82)			Cohort B (N=112)			Cohort C (N=40)		
	ATRX (+)	ATRX (–)	P (intra)	ATRX (+)	ATRX (–)	P (intra)	ATRX (+)	ATRX (–)	P (intra)
Gender			0.142			0.504			0.859
Male	29	18		32	33		9	14	
Female	15	20		27	20		8	9	
WHO			0.001			0.107			0.712
III	2	17		29	35		7	7	
IV	42	21		30	18		10	16	
Age (years), mean ±SD	52.7±12.3	53.6±11.4	0.740	53.6±14.3	54.4±10.9	0.743	45.4±12.4	58.3±15.2	0.001
VASARI, mean ±SD	71.7±5.5	73.5±7.2	0.221	70.7±5.9	72.8±6.2	0.073	71.5±9.3	71.5±6.2	0.984

ATRX, alpha-thalassemia X-linked intellectual disability; WHO, World Health Organization; VASARI, Visually Accessible Rembrandt Images.

nomogram construction, calibration curve analysis, decision curve analysis, and clinical application curve analysis. These evaluations helped to determine the accuracy and applicability of the model in clinical settings.

Statistical analysis

All statistical analyses were performed using R software (version 4.2.0; https://www.r-project.org). The t test or Mann-Whitney test was used for continuous variables, the chi-squared test was used for classifying variables, and the Delong test was used to evaluate the differences between ROC curves. All statistical tests were 2-sided with a statistical significance threshold of $P<0.05$.

Results

Construction of image models

A total of 234 patients (120 *ATRX* mutant type, 114 *ATRX* wild type) were included in this study. The clinical characteristics of these patients are shown in *Table 1*. There were no significant differences in clinical characteristics except for WHO grade in cohort A and age in cohort C. Cohort A and cohort B data were randomly sampled based on gender and WHO grade and were split into a training set (N=155) and validation set (N=39) at a ratio of 4:1 for model development according to the practice of previous machine learning research (the ratio of training set to verification set is generally maintained between 4:1 and 3:1) (26). Cohort C data (N=40) was used as an independent test set for external validation of the model. Through multivariate

LR, 9 imaging models were constructed and 5-fold cross-validation was performed.

Selection of the optimal imaging model

Table 2 summarizes the results of 5-fold cross-validation on the training and validation sets for 9 imaging models, and *Table 3* shows the results of the models on the external test set; all the models shown good predictive performance (AUC >0.75). *Figure 3A,3B* depict the performance of the 6 models constructed from single-type features (radiomics or DL) of 3 ROI regions (edema, tumor, overall), and the models based on overall had a higher AUC relative to the models based on edema and tumor area (overall DL model on the validation set: AUC =0.910, 95% CI: 0.833–0.999; overall radiomics model on the test set: AUC =0.916, 95% CI: 0.819–1.000). In the 3 models based on hybrid features (*Figure 3C,3D*), the model derived from the overall had the best predictive performance (validation set: AUC =0.916, 95% CI: 0.822–0.999; test set: AUC =0.936, 95% CI: 0.859–1.000). After the Delong test, there was no statistical difference between the ROC curves of the 6 models constructed from single-type features (P>0.05; *Figure 4A,4B*). Finally, the overall hybrid model was identified as the optimal imaging model due to it having the highest AUC among all the imaging models. The Delong test of the ROC comparison between the 9 image models can be found in Table S4.

Predictive performance of the overall hybrid model

The overall hybrid model was constructed using 16 imaging features, 10 of which were deep features and 6 radiomics

Table 2 The performance of the models in the training and validation set

Model	Training cohort (N=155)				Validation cohort (N=39)			
	Sensitivity	Specificity	Accuracy	AUC (95% CI)	Sensitivity	Specificity	Accuracy	AUC (95% CI)
Edema DL	0.869	0.819	0.845	0.903 (0.869–0.958)	0.798	0.770	0.789	0.834 (0.645–0.989)
Edema radiomics	0.852	0.802	0.829	0.910 (0.870–0.958)	0.847	0.755	0.804	0.896 (0.774–0.990)
Edema hybrid	0.833	0.804	0.820	0.915 (0.869–0.960)	0.837	0.792	0.814	0.914 (0.842–1.000)
Tumor DL	0.832	0.777	0.807	0.900 (0.849–0.945)	0.814	0.749	0.783	0.880 (0.804–0.996)
Tumor radiomics	0.828	0.779	0.805	0.882 (0.829–0.932)	0.798	0.747	0.773	0.834 (0.672–0.963)
Tumor hybrid	0.872	0.819	0.847	0.929 (0.886–0.965)	0.844	0.798	0.824	0.903 (0.796–0.998)
Overall DL	0.874	0,857	0.866	0.945 (0.904–0.979)	0.859	0.762	0.819	0.910 (0.833–0.999)
Overall radiomics	0.861	0.827	0.845	0.917 (0.879–0.962)	0.829	0.804	0.815	0.898 (0.751–1.000)
Overall hybrid	0.915	0.876	0.897	0.966 (0.948–0.991)	0.852	0.862	0.861	0.916 (0.822–0.999)
Clinical	0.705	0.571	0.643	0.677 (0.586–0.766)	0.658	0.546	0.604	0.641 (0.489–0.796)
Fusion	0.920	0.881	0.902	0.969 (0.964–0.997)	0.925	0.860	0.900	0.956 (0.878–1.000)

AUC, area under curve; CI, confidence interval; edema DL, edema deep learning feature model; edema radiomics, edema radiomics model; edema hybrid, edema radiomics and deep learning feature model; tumor DL, tumor deep learning feature model; tumor radiomics, tumor radiomic model; tumor hybrid, tumor deep learning feature model; overall DL, overall lesion region deep learning feature model; overall radiomics, overall lesion region radiomic model; overall hybrid, overall lesion region radiomics and deep learning feature model; clinical, clinical model; fusion, fusion model.

Table 3 The performance of the models in the test set (N=40)

Models	Sensitivity	Specificity	Accuracy	AUC (95% CI)
Edema DL	0.647	0.783	0.725	0.775 (0.629–0.921)
Edema radiomics	0.765	0.870	0.825	0.875 (0.757–0.992)
Edema hybrid	0.765	0.957	0.875	0.893 (0.789–0.996)
Tumor DL	0.706	0.826	0.775	0.887 (0.788–0.987)
Tumor radiomics	0.647	0.696	0.675	0.818 (0.687–0.950)
Tumor hybrid	0.774	0.869	0.835	0.923 (0.845–1.000)
Overall DL	0.705	0.783	0.750	0.903 (0.814–0.992)
Overall radiomics	0.760	0.827	0.800	0.916 (0.819–1.000)
Overall hybrid	0.824	0.870	0.850	0.936 (0.859–1.000)
Clinical	0.471	0.783	0.650	0.772 (0.624–0.920)
Fusion	0.824	0.913	0.875	0.949 (0.890–1.000)

AUC, area under curve; CI, confidence interval; edema DL, edema deep learning feature model; edema radiomics, edema radiomics model; edema hybrid, edema radiomics and deep learning feature model; tumor DL, tumor deep learning feature model; tumor radiomics, tumor radiomic model; tumor hybrid, tumor deep learning feature model; overall DL, overall lesion region deep learning feature model; overall radiomics, overall lesion region radiomic model; overall hybrid, overall lesion region radiomics and deep learning feature model; clinical, clinical model; fusion, fusion model.
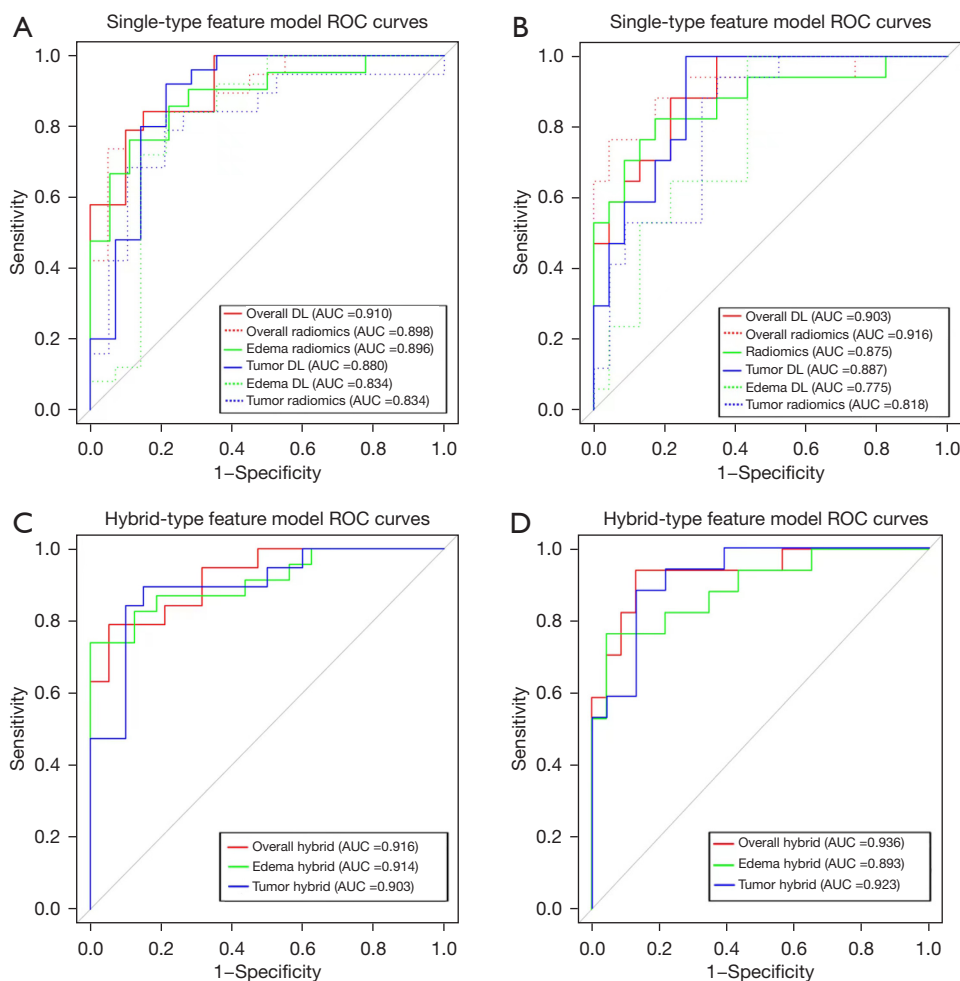
258

Liu et al. A fusion model for predicting ATRX mutation

Figure 3 The comparison of prediction performance of the different models. (A) The ROC curve of the 6 models for the validation set; (B) the ROC curve of the 6 models for the test set; (C) the ROC curve of the 3 models constructed with hybrid features for the validation set; (D) the ROC curve of the 3 models for the test set. ROC, receiver operating characteristic; AUC, area under curve; DL, deep learning.

features. These features were selected from a total of 8,444 features in the overall lesion region. The selection process involved filtering via t test, LASSO, and the backward step search algorithm to prevent overfitting. The resulting features were found to have low correlation with each other (Figure S1), which could indicate that they complemented each other in the model. The classification performance of the model was evaluated in the validation and test sets, as shown in Figure S2. The model demonstrated good performance in accurately classifying lesions, indicating its potential as a diagnostic tool.

Construction and evaluation of the fusion model

The imaging signature was constructed with the overall

hybrid model to calculate the imaging score of each patient (see Appendix 2 for details). The imaging score was then combined with WHO grade, age, sex, and VASARI score to develop a fusion model. The AUC of the fusion model on the training, validation, and test sets were 0.969, 0.956, and 0.949, respectively; the sensitivity was 0.920, 0.925, and 0.824, respectively; the specificity was 0.881, 0.860, and 0.913, respectively; and the accuracy was 0.902, 0.900, and 0.875, respectively. In the training, validation, and test set, the fusion model had the highest AUC value compared to the overall hybrid model and the clinical model, and the overall hybrid model had a higher AUC than did the clinical model (*Tables 2,3*). With the Delong test (*Figure 4C,4D*), there was no significant difference between the fusion model and the overall hybrid model, and both the fusion
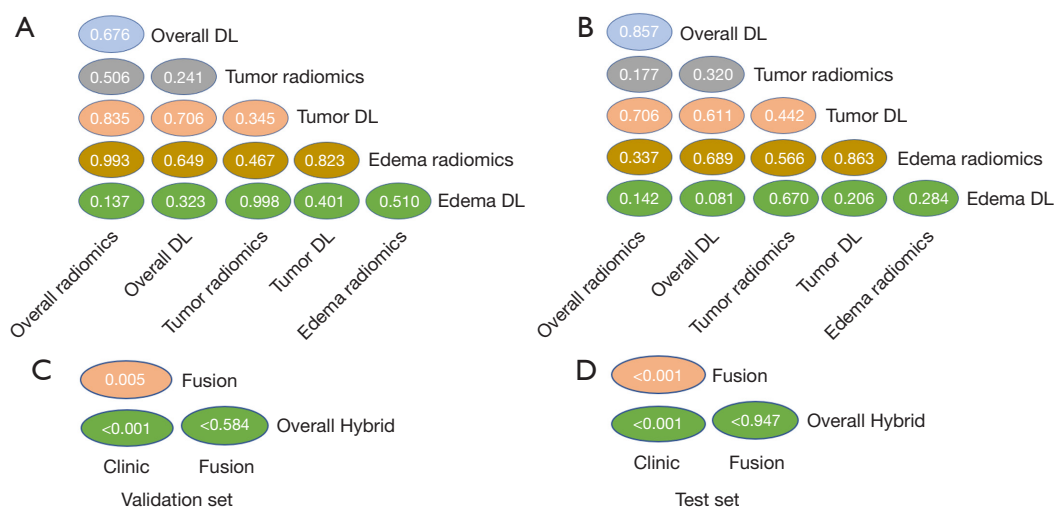
Figure 4 Delong test for the different models. (A) Delong test of 6 models constructed with single-type features for the validation set; (B) Delong test results of the 6 models for the test set; (C) Delong test for the fusion, overall hybrid, and clinical model for the validation set; (D) Delong test for the fusion, overall hybrid, and clinical model for the test set. DL, deep learning.

model and the overall model had significant differences compared to the clinical model, regardless of whether the validation set or a test set was considered.

A clinical nomogram was established using the fusion model to show the value of combining imaging scores and clinical variables to predict the *ATRX* mutation status (*Figure 5A*). The linear predictive value and risk probability of the patient can be obtained from the clinical nomogram. For example, for a 34-year-old female patient, with WHO CNS grade 4, VASARI 77, and imaging score –4, the score of each item is first determined on the Points line according to the patient's information, which is added up to a total score and is further transformed into the linear predictive value and risk probability according to the total score in the Total Points line. In this example, the linear predictive value of the patient is –1, indicating that her risk is relatively low, with a risk probability of 0.25 below the risk threshold and an expected ATRX mutation–negative status. The calibration curves showed good agreement between predictions and observations on the test sets (*Figure 5B*). It was found that the fusion model and the overall hybrid model both had a higher net benefit compared to the clinical model (*Figure 5C*). After the fusion model was simulated in a sample that scaled up to 1,000 for risk stratification, it could be surmised from the clinical impact curve that the fusion model predictions were in good agreement with the actual true-positive results (*Figure 5D*).

Discussion

In this study, we developed a fusion model that integrated the radiomics and DL features derived from cMRI and clinical variables for the noninvasive prediction of *ATRX* mutation status in patients with *IDH*-mutant high-grade astrocytoma. Compared with the imaging models and the clinical model, the fusion model had the best performance. In addition, all imaging models performed better than did the clinic model.

ATRX loss drives glioma-related biological behaviors by directly regulating chromatin structure and composition (27) and favors the malignant progression of gliomas (28). *ATRX* mutations can be used to determine prognosis and even indicate clinicopathological grading (29). The heterogeneity of tumor biological behavior can be captured by MRI image features. Preoperative MRI features have been used to predict *ATRX* mutations in previous studies, but mainly in LGG. Li *et al.* (30) built a T2-weighted imaging-based radiomics model to determine *ATRX* mutations in LGGs and achieved the highest AUC of 0.94. Wu *et al.* (31) predicted *ATRX* mutations in LGGs by combining age, gender, and radiomic features, with a concordance index of 0.863 and 0.840 for the training and test sets, respectively. Calabrese *et al.* (32) assessed 9 genetic biomarkers including *ATRX* in 400 adults with WHO grade 4 gliomas using a radiomic signature, CNN, and a combination of the 2, and the AUC value of *ATRX* reached as high as 0.97. Compared
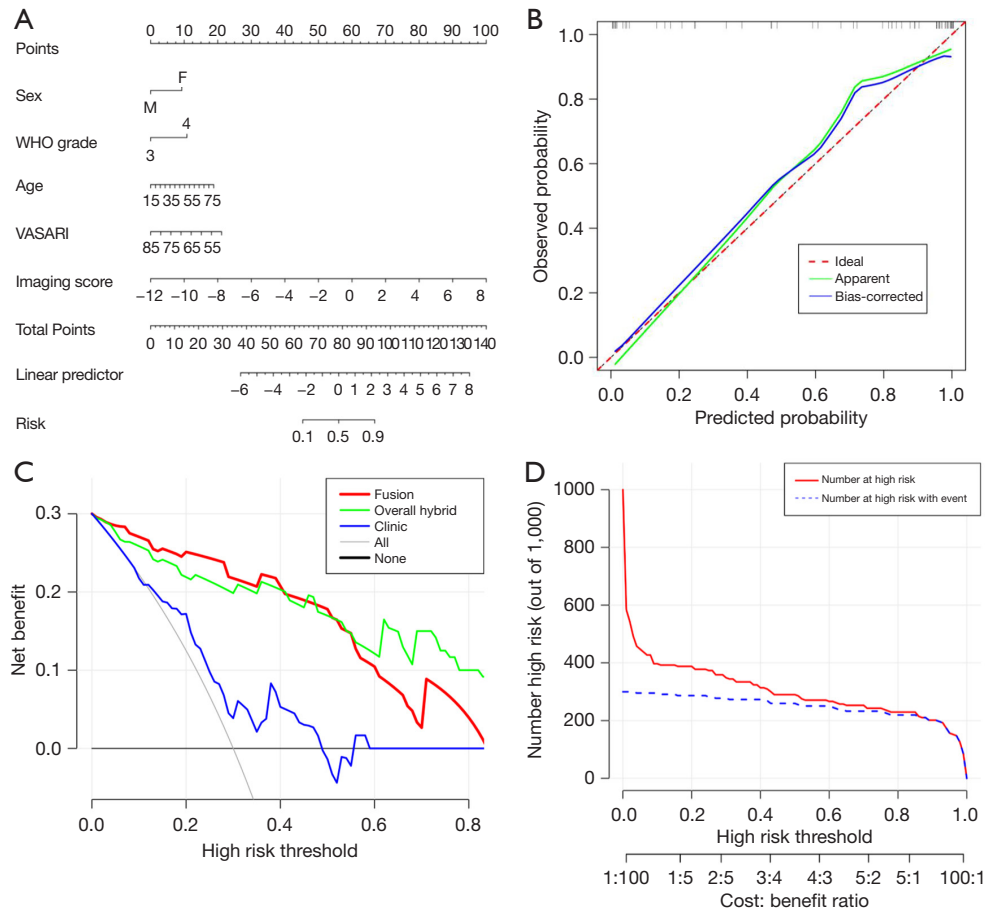
Figure 5 The evaluation of the fusion model. (A) Clinical nomogram established using the fusion model; (B) the calibration curves of the fusion model on the test set; (C) Decision curve analysis of the fusion model, overall hybrid, and the clinic model; (D) the clinical impact curve of the fusion model. The red curve (number at high risk) indicates the number of people who are classified as positive (high risk) by the fusion model at each threshold probability, and the blue curve (number at high risk with event) is the number of true positives at each threshold probability. VASARI, Visually Accessible Rembrandt Images; WHO, World Health Organization.

with previous studies, our study focused more on the *ATRX* mutation of high-grade IDH-mutant astrocytoma, which is more meaningful for clinical treatment. Unlike Calabrese *et al.* (32), who averaged the 2 output probabilities (1 from the CNN limb and 1 from the radiomics limb) to create a final combined model probability, we used CNN to extract deep features of each patient and built an LR model together with traditional radiomics features. Before constructing the model, we fused the features, which allowed us to screen a larger number and variety of features, enhancing the model's flexibility. Additionally, we explored the possibility of using the fused features to predict the status of *ATRX* mutations, which enriches the existing prediction models. In addition, we added qualitative features such as

VASARI, which improved the predictive performance.

Advancements in DL methods have shown superior performance over traditional machine learning methods in predicting tumor genetics and molecular biology based on MRI data (33). The combination of DL and radiomics features has stronger differential ability and is more robust (34). In this study, rather than constructing a direct end-to-end DL model, we extracted highly abstracted semantic features as DL features for the model, and their prediction performance was comparable to, or even surpassed, that of the radiomics features. Out of the 16 image features screened for the optimal image model construction, 10 were derived from DL features. Additionally, the correlation coefficient plots indicated that

the final 16 selected features exhibited a low interfeature correlation but had a high correlation with the outcome variables. This suggests that DL features, unlike radiomics features, can effectively capture the information related to tumor genetics and molecular biology. Hybrid models combining radiomics and DL features outperformed those relying solely on either DL or radiomics features across the training, validation, and test sets. This indicates that DL features play a crucial role in the predictive performance of image models and that radiomics and DL features have complementary roles in the model. While the clinical model incorporating the VASARI score showed limited predictive performance, the fusion model that integrated clinical features with radiomics and DL features demonstrated the best predictive performance. This implies the VASARI score can contributed to predicting *ATRX* mutation status in high-grade *IDH*-mutant astrocytoma.

MRI is the preferred method for the *in vivo* investigation of most brain diseases (35). MRI data analysis techniques enable the exploration of associations between image features and diverse molecular phenotypes. This facilitates a more profound investigation of specific molecular variations and the biological behaviors of gliomas. In this study, using cMRI sequences (T2f and T1c) alone was sufficient to achieve good predictive performance. This can be explained by the ability of T2f to effectively distinguish between different components of tumors and the ability of T1c to reveal important information regarding tumor blood supply and internal features. Furthermore, we found that models based on the overall lesion features outperformed those based solely on edema and enhancing tumor area. This suggests that the combination of T1c and T2f can characterize the glioma-specific changes caused by *ATRX* mutations.

In this study, we fully leveraged the information garnered from cMRI and innovatively used it to predict the *ATRX* mutation status of patients with high-grade *IDH*-mutant astrocytoma, achieving promising results. Nevertheless, this study had several limitations that should be addressed and improved upon. First, although the model we developed was based on a multicenter study and showed good performance in the external validation, the sample size was not sufficiently large. Larger sample sizes and prospective studies are still required to validate this model. Second, although our model based on cMRI showed promising potential, further research should explore whether more interpretable qualitative or semiquantitative features from functional MRI sequences could enhance the prediction of *ATRX* status in *IDH*-mutant high-grade gliomas. Finally,

the manual segmentation methods used to obtain the ROIs were highly time-consuming. Therefore, future research should focus on developing semiautomatic or automatic segmentation methods to obtain ROIs, which could also potentially improve the prediction accuracy.

Conclusions

We developed a multicenter clinical trait-imaging fusion model that combines MRI radiomics and DL features with clinical variables, including VASARI features. The model could effectively predict the *ATRX* mutation status of patients with *IDH*-mutant high-grade astrocytoma based on cMRI and may thus aid in the development of more targeted and effective treatment strategies.

Acknowledgments

Footnote

Reporting Checklist: The authors have completed the TRIPOD reporting checklist. Available at https://qims.amegroups.com/article/view/10.21037/qims-23-807/rc

Conflicts of Interest: All authors have completed the ICMJE uniform disclosure form (available at https://qims.amegroups.com/article/view/10.21037/qims-23-807/coif). The authors have no conflicts of interest to declare.

Ethical Statement: The authors are accountable for all aspects of the work in ensuring that questions related to the accuracy or integrity of any part of the work are appropriately investigated and resolved. The study was conducted in accordance with the Declaration of Helsinki (as revised in 2013) and was approved by the institutional review boards of Chongqing Medical University, Sichuan Cancer Hospital, and the United Medical Imaging Center. All participating institutions were formally informed of and agreed to the study protocol. Given the retrospective nature of the design, the requirements for informed consent from patients was waived.

Open Access Statement: This is an Open Access article distributed in accordance with the Creative Commons

References

1. Pladevall-Morera D, Castejón-Griñán M, Aguilera P, Gaardahl K, Ingham A, Brosnan-Cashman JA, Meeker AK, Lopez-Contreras AJ. ATRX-Deficient High-Grade Glioma Cells Exhibit Increased Sensitivity to RTK and PDGFR Inhibitors. Cancers (Basel) 2022;14:1790.

2. Reardon DA, Wen PY. Glioma in 2014: unravelling tumour heterogeneity-implications for therapy. Nat Rev Clin Oncol 2015;12:69-70.

3. Louis DN, Perry A, Wesseling P, Brat DJ, Cree IA, Figarella-Branger D, Hawkins C, Ng HK, Pfister SM, Reifenberger G, Soffietti R, von Deimling A, Ellison DW. The 2021 WHO Classification of Tumors of the Central Nervous System: a summary. Neuro Oncol 2021;23:1231-51.

4. Louis DN, Perry A, Reifenberger G, von Deimling A, Figarella-Branger D, Cavenee WK, Ohgaki H, Wiestler OD, Kleihues P, Ellison DW. The 2016 World Health Organization Classification of Tumors of the Central Nervous System: a summary. Acta Neuropathol 2016;131:803-20.

5. Han B, Cai J, Gao W, Meng X, Gao F, Wu P, Duan C, Wang R, Dinislam M, Lin L, Kang C, Jiang C. Loss of ATRX suppresses ATM dependent DNA damage repair by modulating H3K9me3 to enhance temozolomide sensitivity in glioma. Cancer Lett 2018;419:280-90.

6. Weller M, van den Bent M, Preusser M, Le Rhun E, Tonn JC, Minniti G, et al. EANO guidelines on the diagnosis and treatment of diffuse gliomas of adulthood. Nat Rev Clin Oncol 2021;18:170-86.

7. Ceccarelli M, Barthel FP, Malta TM, Sabedot TS, Salama SR, Murray BA, et al. Molecular Profiling Reveals Biologically Discrete Subsets and Pathways of Progression in Diffuse Glioma. Cell 2016;164:550-63.

8. Purkait S, Miller CA, Kumar A, Sharma V, Pathak P, Jha P, Sharma MC, Suri V, Suri A, Sharma BS, Fulton RS, Kale SS, Dahiya S, Sarkar C. ATRX in Diffuse Gliomas With its Mosaic/Heterogeneous Expression in a Subset. Brain Pathol 2017;27:138-45.

9. Di Bonaventura R, Montano N, Giordano M, Gessi M, Gaudino S, Izzo A, Mattogno PP, Stumpo V, Caccavella VM, Giordano C, Lauretti L, Colosimo C, D'Alessandris QG, Pallini R, Olivi A. Reassessing the Role of Brain Tumor Biopsy in the Era of Advanced Surgical, Molecular, and Imaging Techniques-A Single-Center Experience with Long-Term Follow-Up. J Pers Med 2021;11:909.

10. Wangaryattawanich P, Hatami M, Wang J, Thomas G, Flanders A, Kirby J, Wintermark M, Huang ES, Bakhtiari AS, Luedi MM, Hashmi SS, Rubin DL, Chen JY, Hwang SN, Freymann J, Holder CA, Zinn PO, Colen RR. Multicenter imaging outcomes study of The Cancer Genome Atlas glioblastoma patient cohort: imaging predictors of overall and progression-free survival. Neuro Oncol 2015;17:1525-37.

11. Gevaert O, Mitchell LA, Achrol AS, Xu J, Echegaray S, Steinberg GK, Cheshier SH, Napel S, Zaharchuk G, Plevritis SK. Glioblastoma Multiforme: Exploratory Radiogenomic Analysis by Using Quantitative Image Features. Radiology 2015;276:313.

12. Lambin P, Leijenaar RTH, Deist TM, Peerlings J, de Jong EEC, van Timmeren J, Sanduleanu S, Larue RTHM, Even AJG, Jochems A, van Wijk Y, Woodruff H, van Soest J, Lustberg T, Roelofs E, van Elmpt W, Dekker A, Mottaghy FM, Wildberger JE, Walsh S. Radiomics: the bridge between medical imaging and personalized medicine. Nat Rev Clin Oncol 2017;14:749-62.

13. He K, Zhang X, Ren S, Sun J. Deep Residual Learning for Image Recognition. Las Vegas, NV, USA: 2016 IEEE Conference on Computer Vision and Pattern Recognition (CVPR); IEEE, 2016.

14. Chen LC, Papandreou G, Kokkinos I, Murphy K, Yuille AL. DeepLab: Semantic Image Segmentation with Deep Convolutional Nets, Atrous Convolution, and Fully Connected CRFs. IEEE Trans Pattern Anal Mach Intell 2018;40:834-48.

15. Buda M, AlBadawy EA, Saha A, Mazurowski MA. Deep Radiogenomics of Lower-Grade Gliomas: Convolutional Neural Networks Predict Tumor Genomic Subtypes Using MR Images. Radiol Artif Intell 2020;2:e180050.

16. Matsui Y, Maruyama T, Nitta M, Saito T, Tsuzuki S, Tamura M, Kusuda K, Fukuya Y, Asano H, Kawamata T, Masamune K, Muragaki Y. Prediction of lower-grade glioma molecular subtypes using deep learning. J Neurooncol 2020;146:321-7.

17. Li G, Li L, Li Y, Qian Z, Wu F, He Y, Jiang H, Li R, Wang D, Zhai Y, Wang Z, Jiang T, Zhang J, Zhang W. An MRI radiomics approach to predict survival and tumour-infiltrating macrophages in gliomas. Brain 2022;145:1151-61.

18. Chen S, Xu Y, Ye M, Li Y, Sun Y, Liang J, Lu J, Wang Z, Zhu Z, Zhang X, Zhang B. Predicting MGMT Promoter

Methylation in Diffuse Gliomas Using Deep Learning with Radiomics. J Clin Med 2022;11:3445.

19. Choi YS, Bae S, Chang JH, Kang SG, Kim SH, Kim J, Rim TH, Choi SH, Jain R, Lee SK. Fully automated hybrid approach to predict the IDH mutation status of gliomas via deep learning and radiomics. Neuro Oncol 2021;23:304-13.

20. Ren Y, Zhang X, Rui W, Pang H, Qiu T, Wang J, Xie Q, Jin T, Zhang H, Chen H, Zhang Y, Lu H, Yao Z, Zhang J, Feng X. Noninvasive Prediction of IDH1 Mutation and ATRX Expression Loss in Low-Grade Gliomas Using Multiparametric MR Radiomic Features. J Magn Reson Imaging 2019;49:808-17.

21. Zhang L, Pan H, Liu Z, Gao J, Xu X, Wang L, Wang J, Tang Y, Cao X, Kan Y, Wen Z, Chen J, Huang D, Chen S, Li Y. Multicenter clinical radiomics-integrated model based on [18F]FDG PET and multi-modal MRI predict ATRX mutation status in IDH-mutant lower-grade gliomas. Eur Radiol 2023;33:872-83.

22. Avants BB, Tustison NJ, Song G, Cook PA, Klein A, Gee JC. A reproducible evaluation of ANTs similarity metric performance in brain image registration. Neuroimage 2011;54:2033-44.

23. Shinohara RT, Sweeney EM, Goldsmith J, Shiee N, Mateen FJ, Calabresi PA, Jarso S, Pham DL, Reich DS, Crainiceanu CM; Australian Imaging Biomarkers Lifestyle Flagship Study of Ageing; Alzheimer's Disease Neuroimaging Initiative. Statistical normalization techniques for magnetic resonance imaging. Neuroimage Clin. 2014;6:9-19. Erratum in: Neuroimage Clin 2015;7:848.

24. Fedorov A, Beichel R, Kalpathy-Cramer J, Finet J, Fillion-Robin JC, Pujol S, Bauer C, Jennings D, Fennessy F, Sonka M, Buatti J, Aylward S, Miller JV, Pieper S, Kikinis R. 3D Slicer as an image computing platform for the Quantitative Imaging Network. Magn Reson Imaging 2012;30:1323-41.

25. Wei J, Yang G, Hao X, Gu D, Tan Y, Wang X, Dong D, Zhang S, Wang L, Zhang H, Tian J. A multi-sequence and habitat-based MRI radiomics signature for preoperative prediction of MGMT promoter methylation in astrocytomas with prognostic implication. Eur Radiol 2019;29:877-88.

26. Raschka S. Model Evaluation, Model Selection, and Algorithm Selection in Machine Learning. doi: 10.48550/arXiv.1811.12808.

27. Danussi C, Bose P, Parthasarathy PT, Silberman PC, Van Arnam JS, Vitucci M, Tang OY, Heguy A, Wang Y, Chan TA, Riggins GJ, Sulman EP, Lang FF, Creighton CJ, Deneen B, Miller CR, Picketts DJ, Kannan K, Huse JT. Atrx inactivation drives disease-defining phenotypes in glioma cells of origin through global epigenomic remodeling. Nat Commun 2018;9:1057.

28. Wang Y, Yang J, Wild AT, Wu WH, Shah R, Danussi C, Riggins GJ, Kannan K, Sulman EP, Chan TA, Huse JT. G-quadruplex DNA drives genomic instability and represents a targetable molecular abnormality in ATRX-deficient malignant glioma. Nat Commun 2019;10:943.

29. Xie Y, Tan Y, Yang C, Zhang X, Xu C, Qiao X, Xu J, Tian S, Fang C, Kang C. Omics-based integrated analysis identified ATRX as a biomarker associated with glioma diagnosis and prognosis. Cancer Biol Med 2019;16:784-96.

30. Li Y, Liu X, Qian Z, Sun Z, Xu K, Wang K, Fan X, Zhang Z, Li S, Wang Y, Jiang T. Genotype prediction of ATRX mutation in lower-grade gliomas using an MRI radiomics signature. Eur Radiol 2018;28:2960-8.

31. Wu S, Zhang X, Rui W, Sheng Y, Yu Y, Zhang Y, Yao Z, Qiu T, Ren Y. A nomogram strategy for identifying the subclassification of IDH mutation and ATRX expression loss in lower-grade gliomas. Eur Radiol 2022;32:3187-98.

32. Calabrese E, Rudie JD, Rauschecker AM, Villanueva-Meyer JE, Clarke JL, Solomon DA, Cha S. Combining radiomics and deep convolutional neural network features from preoperative MRI for predicting clinically relevant genetic biomarkers in glioblastoma. Neurooncol Adv 2022;4:vdac060.

33. Bangalore Yogananda CG, Shah BR, Vejdani-Jahromi M, Nalawade SS, Murugesan GK, Yu FF, Pinho MC, Wagner BC, Mickey B, Patel TR, Fei B, Madhuranthakam AJ, Maldjian JA. A novel fully automated MRI-based deep-learning method for classification of IDH mutation status in brain gliomas. Neuro Oncol 2020;22:402-11.

34. Ding J, Zhao R, Qiu Q, Chen J, Duan J, Cao X, Yin Y. Developing and validating a deep learning and radiomic model for glioma grading using multiplanar reconstructed magnetic resonance contrast-enhanced T1-weighted imaging: a robust, multi-institutional study. Quant Imaging Med Surg 2022;12:1517-28.

35. Esmaeili M, Vettukattil R, Banitalebi H, Krogh NR, Geitung JT. Explainable Artificial Intelligence for Human-Machine Interaction in Brain Tumor Localization. J Pers Med 2021;11:1213.

Table S1 VASARI scoring standard (according to the National Cancer Institute version; https://wiki.nci.nih.gov/display/cip/vasari)

Feature number	Name	Description	Options
F1	Tumor location	Location of lesion geographic epicenter (not all areas of involvement).	0 = – 1= Frontal 2 =Temporal 3=Insular 4=Parietal 5=Occipital 6=Brainstem 7=Cerebellum
F2	Side of tumor epicenter	Side of lesion epicenter.	0= – 1=Right 2=Center/Bilateral 3=Left
F3	Eloquent brain	Does the geographic center or the enhancing component involve eloquent cortex (motor, language, vision) or key underlying white matter?	0= – 1=None 2=Speech motor 3=Speech receptive 4=Motor 5=Vision
F4	Enhancement quality	[None, mild, moderate, marked] Qualitative degree of contrast enhancement is defined as having all or portions of the tumor demonstrating significantly higher signal on the postcontrast T1-weighted images compared to precontrast.	0= – 1=None 2=Mild/Minimal 3=Marked/Avid
F5	Proportion enhancing	[Indeterminate, none (0%), <5%, 6–33%, 34–67%, 68–95%, >95%, all (100%)] What proportion of the entire tumor is enhancing? (assuming that the entire abnormality may be composed of (1) an enhancing component, (2) a nonenhancing component, (3) a necrotic component, or (4) an edema component).	0= – 1= N/A 2=None (0%) 3= <5% 4= 6–33% 5= 34–67% 6= 68–95% 7: >95% 8=All (100%) 9= Indeterminate
F6	Proportion nCET	[Indeterminate, none (0%), <5%, 6–33%, 34–67%, 68–95%, >95%, all (100%)] What proportion of the entire tumor is nonenhancing? Nonenhancing tumor is defined as a region within the tumor that does not enhance but is T2 hyperintense (less than the intensity of cerebrospinal fluid, with corresponding T1-weighted hypointensity) that are associated with mass effect and architectural distortion, including blurring of the gray–white interface (assuming that the entire abnormality may be composed of (1) an enhancing component, (2) a nonenhancing component, (3) a necrotic component, or (4) an edema component).	0= – 1= N/A 2=None (0%) 3= <5% 4= 6–33% 5= 34–67% 6= 68–95% 7: >95% 8=All (100%) 9= Indeterminate
F7	Proportion necrosis	[Indeterminate, none (0%), <5%, 6–33%, 34–67%, 68–95%, >95%, (100%)] All necrosis is defined as a region within the tumor that does not enhance or shows markedly diminished enhancement, is high on T2-weighted and proton-density images, is low on T1-weighted images, and has an irregular border (assuming that the entire abnormality may be composed of (1) an enhancing component, (2) a nonenhancing component, (3) a necrotic component, or (4) an edema component).	0= – 1= N/A 2=None (0%) 3= <5% 4= 6–33% 5= 34–67% 6= 68–95% 7: >95% 8=All (100%) 9= Indeterminate
F8	Cyst(s)	Cysts are well defined, rounded, and often eccentric regions of very high T2-weighted signal and low T1-weighted signal essentially matching CSF signal intensity, with very thin, regular, smooth, and nonenhancing or regularly enhancing walls, possibly with thin, regular, internal septations.	0= – 1= No 2= Yes
F9	Multifocal or multicentric	Multifocal is defined as having at least 1 region of tumor, either enhancing or nonenhancing, that is not contiguous with the dominant lesion and is outside the region of signal abnormality (edema) surrounding the dominant mass. This can be defined as those resulting from dissemination or growth by an established route, spread via commissural or other pathways, or via CSF channels or local metastases. Meanwhile, multicentric is defined as widely separated lesions in different lobes or different hemispheres that cannot be attributed to one of the previously mentioned pathways. Gliomatosis refers to generalized neoplastic transformation of the white matter of most of a hemisphere.	0 = – 1= N/A 2= Multifocal 3=Multicentric 4= Gliomatosis
F10	T1/FLAIR ratio	Tumor feature summary [mixed, expansive, or infiltrative]. Expansive = size of precontrast T1 abnormality (exclusive of signal intensity) approximates size of FLAIR abnormality; mixed = size of T1 abnormality moderately less than the FLAIR envelope; infiltrative = size of precontrast T1 abnormality much smaller than the size of the FLAIR abnormality (use T2 if FLAIR is not provided).	0= – 1= Expansive (T1=FLAIR) 2= Mixed (T1<FLAIR) 3= Infiltrative (T1<<FLAIR)
F11	Thickness of enhancing margin	The scoring is not applicable if there is no contrast enhancement. If most of the enhancing rim is thin and regular and has homogeneous enhancement, the grade is thin. If most of the rim demonstrates nodular and/or thick enhancement, the grade is thick. If there is only solid enhancement and no rim, the grade is none.	0= – 1= N/A 2= None 3= Thin 4= Thick/solid
F12	Definition of the enhancing margin	The scoring is not applicable (N/A) if there is no contrast enhancement. Assess if most of the outside margin of the enhancement is well defined or poorly defined.	0= – 1= N/A 2= Well-defined 3= Poorly–defined
F13	Definition of the nonenhancing margin (e.g., grade III)	If most of the outside nonenhancing margin of the tumor is well defined and smooth (geographic), versus if the margin is ill-defined and irregular.	0= – 1= N/A 2= Smooth 3= Irregular
F14	Proportion of edema	[Indeterminate, none (0%), <5%, 6–33%, 34–67%, 68–95%, >95%, all (100%)]. What proportion of the entire abnormality is vasogenic edema? Edema should be greater in signal than in nCET and somewhat lower in signal than in CSF. Pseudopods are characteristic of edema (assuming that the entire abnormality may be composed of (1) an enhancing component, (2) a nonenhancing component, (3) a necrotic component, or (4) an edema component).	0= – 1= N/A 2=None (0%) 3= <5% 4= 6–33% 5= 34–67% 6= 68–95% 7: >95% 8=All (100%) 9=Indeterminate
F15	Crosses edema	Edema spans white matter commissures extending into the contralateral hemisphere. (exclusive of herniated ipsilateral tissue).	0= – 1= N/A 2= No 3= Yes
F16	Hemorrhage	Intrinsic hemorrhage in the tumor matrix. Any intrinsic foci of low signal on T2-weighted imaging or high signal on T1-weighted imaging. (Use Bo image if necessary for confirmation.)	0= – 1= N/A 2= No 3= Yes
F17	Diffusion	Predominantly facilitated or restricted diffusion in the enhancing or nCET portion of the tumor (based on ADC map). Equivocal is neither. If there is no ADC, use no images. The proportion of tissue is not relevant.	0= – 1= No image 2= Facilitated 3= Restricted 4=Neither/equivocal
F18	Pial invasion	Enhancement of the overlying pia in continuity with enhancing or nonenhancing tumor.	0= – 1= No 2= Yes
F19	Ependymal invasion	Invasion of any adjacent ependymal surface in continuity with enhancing or nonenhancing tumor matrix.	0= – 1= No 2= Yes
F20	Cortical involvement	Nonenhancing or enhancing tumor extending into the cortical mantle or the cortex no longer distinguishable relative to subjacent tumor.	0= – 1= No 2= Yes
F21	Deep WM invasion	Enhancing or nCET tumor extending into the internal capsule or brainstem.	0= – 1= No 2= Yes
F22	nCET tumor crosses midline	nCET crossing into the contralateral hemisphere through white matter commissures (exclusive of herniated ipsilateral tissue).	0= – 1= N/A 2= No 3= Yes
F23	Enhancing tumor crosses midline	Enhancing tissue crossing into the contralateral hemisphere through white matter commisures (exclusive of herniated ipsilateral tissue).	0= – 1= N/A 2= No 3= Yes
F24	Satellites	An area of enhancement within the region of signal abnormality surrounding the dominant lesion but not contiguous with any part with the major tumor mass.	0= – 1= No 2= Yes
F25	Calvarial remodeling	Erosion of the inner table of the skull (possibly a secondary sign of slow growth).	0= – 1= No 2= Yes
F26	Extent of resection of enhancing tumor	[Indeterminate, none (0%), <5%, 6–33%, 34–67%, 68–33%, 34–67%, 68–95%, >95%, all (100%)]. Use the first postoperative scan (contrast- enhanced MR imaging) assessed for residual tumor. Estimate the proportion of enhancing tumor removed. A total resection of the component should be scored 100%. A subtotal resection of enhancing tissue should be scored accordingly.	0= – 1= N/A 2=None (0%) 3= <5% 4= 6–33% 5= 34–67% 6= 68–95% 7: >95% 8=All (100%) 9=Indeterminate
F27	Extent resection of nCET	[Indeterminate, none (0%), <5%, 6–33%, 34–67%, 68–95%, >95%, all (100%)]. Use the first postoperative scan (contrast-enhanced MR imaging) assessed for tumor residual. Estimate the proportion of non-enhancing tumor removed. A total resection of component should be scored 100%. A subtotal resection of enhancing tissue should be scored accordingly.	0= – 1= N/A 2=None (0%) 3= <5% 4= 6–33% 5= 34–67% 6= 68–95% 7: >95% 8=All (100%) 9=Indeterminate
F28	Extent resection of vasogenic edema	[Indeterminate, none (0%), <5%, 6–33%, 34–67%, 68–95%, >95%, all (100%)]Use the first postoperative scan (contrast-enhanced MR imaging) assessed for residual tumor. Estimate the proportion of edema removed. A total resection of enhancing nidus should be scored 100%. A subtotal resection of enhancing tissue should be scored accordingly.	0= – 1= N/A 2=None (0%) 3= <5% 4= 6–33% 5= 34–67% 6= 68–95% 7: >95% 8=All (100%) 9= Indeterminate
F29, F30	Lesion size	Largest perpendicular (x–y) cross-sectional diameter of T2 signal abnormality (longest dimension × perpendicular dimension) measured on a single axial image only.	0= – 1= <0.5cm 2= 0.5 cm 3= 1.0 cm 4= 1.5 cm 5= 2.0 cm 6= 2.5 cm 7= 3.0 cm 8= 3.5 cm 9= 4.0 cm 10= 4.5 cm 11= 5.0 cm 12 = 5.5 cm 13= 6.0 cm 14= 6.5 cm 15= 7.0 cm 16= 7.5 cm 17= 8.0 cm 18= >8.0 cm

VASARI, visually accessible Rembrandt images; CSF, cerebrospinal fluid; FLAIR, fluid attenuated inversion recovery; ADC, apparent diffusion coefficient.

Table S2 MRI image acquisition protocol parameters from 3 centers

Parameters	A	B	C
Scanner type	GE Signa HDxt 3.0T (GE Medical Systems, Chicago, IL, USA)	Siemens Skyra 3.0T (Siemens Healthineers, Erlangen, Germany)	GE Discovery MR750 3.0T (GE Medical Systems, Chicago, IL, USA)
Magnetic field strength	3.0T	3.0T	3.0T
T1C (T1 contrast enhanced)			
Repetition time (ms)	225	459	549
Echo time (ms)	4.8	3	5.72
Flip angle (º)	90	90	90
Image slice thickness (mm)	2	2	2
Image slice spacing (mm)	1	0.5	1
T2f (T2-FLAIR)			
Repetition time (ms)	8,000	7,000	8,000
Echo time (ms)	101	79	100
Flip angle (º)	150	180	110
Image slice thickness (mm)	5	5	5
Image slice spacing (mm)	5	2	2

MRI, magnetic resonance imaging; GE, General Electric Company; T1C, T1-contrast enhanced; T2f, T2 fluid attenuated inversion recovery.

Table S3 Clinical variables

Index	Label (ATRX mutant =1, ATRX wild type =0)	Age (years)	Gender	WHO grade	VASARI score
000-1	0	34	F	4	77
000-2	0	34	M	4	78
000-3	0	64	M	4	77
000-4	0	50	F	3	75
000-5	0	53	M	4	80
000-6	0	57	M	3	66
000-7	0	65	M	4	84
000-8	0	65	F	3	67
000-9	0	69	F	3	68
000-10	0	50	F	3	62
000-11	0	67	F	3	84
000-12	0	56	M	3	76
000-13	0	64	M	3	78
000-14	0	70	F	4	66
000-15	0	55	M	3	74
000-16	0	55	F	4	78
000-17	0	57	M	4	81
000-18	0	45	M	4	71
000-19	0	51	M	4	66
000-20	0	53	F	3	78
000-21	0	65	F	3	80
000-22	0	46	F	3	80
000-23	0	60	F	4	72
000-24	0	34	M	4	69
000-25	0	36	M	4	58
000-26	0	33	F	4	78
000-27	0	79	M	3	84
000-28	0	43	F	4	76
000-29	0	56	F	4	64
000-30	0	45	F	3	79
000-31	0	39	M	4	72
000-32	0	46	M	4	75
000-33	0	49	M	4	84
000-34	0	67	F	3	58
000-35	0	58	F	4	65
000-36	0	59	M	4	70
000-37	0	58	F	3	66
000-38	0	49	F	3	76
000-39	0	40	M	3	65
000-40	0	27	F	3	66
000-41	0	40	M	3	67
000-42	0	41	M	3	69
000-43	0	66	F	3	72
000-44	0	65	M	3	67
000-45	0	48	F	3	83
000-46	0	42	F	3	77
000-47	0	57	M	3	75
000-48	0	34	F	4	67
000-49	0	65	F	3	78
000-50	0	64	M	3	65
000-51	0	54	F	4	66
000-52	0	66	M	4	67
000-53	0	43	M	3	78
000-54	0	44	M	4	80
000-55	0	54	F	4	81
000-56	0	55	M	3	67
000-57	0	43	M	4	77
000-58	0	45	F	3	78
000-59	0	60	M	3	67
000-60	0	55	M	4	69
000-61	0	65	F	3	77
000-62	0	44	M	4	68
000-63	0	56	M	3	64
000-64	0	67	M	4	71
000-65	0	65	F	3	62
000-66	0	66	M	4	72
000-67	0	67	M	3	74
000-68	0	70	M	3	83
000-69	0	50	F	3	88
000-70	0	51	M	3	85
000-71	0	61	F	4	66
000-72	0	67	M	3	69
000-73	0	56	M	3	81
000-74	0	60	M	4	69
000-75	0	64	M	3	74
000-76	0	70	F	4	69
000-77	0	76	M	4	69
000-78	0	51	M	3	77
000-79	0	41	M	3	72
000-80	0	57	F	4	69

Table S3 *(continued)*

Table S3 *(continued)*

Index	Label (ATRX mutant =1, ATRX wild type =0)	Age (years)	Gender	WHO grade	VASARI score
000-81	0	41	F	3	71
000-82	0	54	F	3	79
000-83	0	61	M	3	76
000-84	0	43	F	3	65
000-85	0	44	M	3	78
000-86	0	69	F	3	69
000-87	0	54	M	4	71
000-88	0	56	M	4	75
000-89	0	54	F	3	83
000-90	0	50	M	4	78
000-91	0	43	M	3	72
000-92	0	21	F	3	62
000-93	0	67	M	4	73
000-94	0	36	F	3	69
000-95	0	61	M	4	78
000-96	0	52	M	3	70
000-97	0	23	M	4	69
000-98	0	58	F	4	72
000-99	0	70	M	4	75
000-100	0	57	M	4	69
000-101	0	51	M	4	71
000-102	0	74	F	4	80
000-103	0	52	F	3	70
000-104	0	76	F	4	83
000-105	0	72	F	4	79
000-106	0	56	M	3	58
000-107	0	56	M	3	62
000-108	0	68	M	4	71
000-109	0	66	F	4	75
000-110	0	52	F	4	80
000-111	0	57	M	3	66
000-112	0	74	M	4	70
000-113	0	78	M	4	69
000-114	0	63	M	4	74
100-1	1	64	M	4	69
100-2	1	53	M	4	69
100-3	1	61	F	4	69
100-4	1	41	M	4	66
100-5	1	53	M	4	76
100-6	1	45	M	4	78
100-7	1	34	F	4	78
100-8	1	66	M	4	65
100-9	1	71	M	4	75
100-10	1	52	M	4	73
100-11	1	66	M	4	64
100-12	1	36	M	4	75
100-13	1	50	M	4	66
100-14	1	54	M	4	77
100-15	1	49	M	4	76
100-16	1	30	F	4	69
100-17	1	67	M	4	65
100-18	1	55	M	4	78
100-19	1	49	M	4	66
100-20	1	50	M	4	68
100-21	1	72	M	4	70
100-22	1	57	M	4	77
100-23	1	46	F	4	69
100-24	1	57	M	4	71
100-25	1	30	M	4	80
100-26	1	45	F	4	68
100-27	1	47	M	4	77
100-28	1	55	M	4	78
100-29	1	51	F	4	63
100-30	1	48	F	4	76
100-31	1	58	Gender	4	75
100-32	1	52	F	4	66
100-33	1	70	F	4	66
100-34	1	66	M	4	67
100-35	1	52	M	3	79
100-36	1	18	F	4	78
100-37	1	49	M	4	64
100-38	1	73	F	4	72
100-39	1	73	F	4	77
100-40	1	51	M	3	65
100-41	1	46	F	4	74
100-42	1	37	F	4	71
100-43	1	56	M	4	66
100-44	1	64	F	4	84

Table S3 *(continued)*

Table S3 *(continued)*

Index	Label (ATRX mutant =1, ATRX wild type =0)	Age (years)	Gender	WHO grade	VASARI score
100-45	1	76	F	4	70
100-46	1	63	F	4	78
100-47	1	54	F	3	73
100-48	1	50	F	4	67
100-49	1	50	M	3	73
100-50	1	85	M	4	74
100-51	1	51	M	4	70
100-52	1	49	M	3	78
100-53	1	74	M	4	65
100-54	1	33	F	4	65
100-55	1	51	M	4	55
100-56	1	54	M	3	74
100-57	1	55	M	3	65
100-58	1	68	F	3	59
100-59	1	55	F	4	69
100-60	1	59	M	3	71
100-61	1	53	F	3	69
100-62	1	54	M	3	71
100-63	1	40	F	3	68
100-64	1	48	M	3	68
100-65	1	51	M	3	71
100-66	1	25	F	3	73
100-67	1	48	F	3	68
100-68	1	63	F	3	54
100-69	1	53	F	4	73
100-70	1	56	M	4	69
100-71	1	64	F	4	70
100-72	1	39	F	3	67
100-73	1	61	M	4	71
100-74	1	58	M	3	72
100-75	1	52	M	3	67
100-76	1	44	M	3	65
100-77	1	58	M	3	65
100-78	1	53	F	3	68
100-79	1	58	M	4	69
100-80	1	46	F	4	81
100-81	1	63	F	4	77
100-82	1	56	M	3	73
100-83	1	54	F	3	69
100-84	1	77	M	3	74
100-85	1	25	F	3	76
100-86	1	66	M	4	76
100-87	1	67	F	4	65
100-88	1	73	M	4	84
100-89	1	71	M	4	67
100-90	1	50	M	3	69
100-91	1	55	M	4	77
100-92	1	71	F	4	71
100-93	1	53	M	4	71
100-94	1	52	M	4	69
100-95	1	26	F	3	74
100-96	1	75	M	4	68
100-97	1	53	F	4	65
100-98	1	60	F	4	72
100-99	1	50	M	4	84
100-100	1	16	F	4	77
100-101	1	16	M	3	67
100-102	1	40	M	3	80
100-103	1	41	F	4	81
100-104	1	48	F	3	63
100-105	1	46	M	3	70
100-106	1	38	M	4	82
100-107	1	50	M	3	68
100-108	1	53	F	4	69
100-109	1	26	Gender	4	76
100-110	1	33	F	3	65
100-111	1	44	M	4	77
100-112	1	46	M	3	52
100-113	1	17	F	4	75
100-114	1	53	M	4	77
100-115	1	54	F	4	80
100-116	1	40	M,	4	84
100-117	1	64	F	4	75
100-118	1	40	M	3	60
100-119	1	63	M	4	83
100-120	1	57	F	3	59

ATRX, alpha-thalassemia X-linked intellectual disability; WHO, World Health Organization; VASARI, visually accessible Rembrandt images; F, female; M, male.

Table S4 The result of Delong test

| Corresponding to different models	Training set	Validation set
Edema DL——edema radio	0.51	0.284
Edema DL——edema hybrid	0.266	0.153
Edema DL——tumor DL	0.401	0.206
Edema DL——tumor radio	0.998	0.67
Edema DL——tumor hybrid	0.427	0.074
Edema DL——overall DL	z	0.081
Edema DL——overall radio	0.137	0.142
Edema DL——overall hybrid	0.338	0.072
Edema radio——edema hybrid	0.569	0.469
Edema radio——tumor DL	0.823	0.863
Edema radio——tumor radio	0.467	0.566
Edema radio——tumor hybrid	0.854	0.52
Edema radio——overall DL	0.649	0.689
Edema radio——overall radio	0.993	0.337
Edema radio——overall hybrid	0.709	0.127
Edema hybrid——tumor DL	0.733	0.941
Edema hybrid——tumor radio	0.099	0.443
Edema hybrid——tumor hybrid	0.708	0.665
Edema hybrid——overall DL	0.912	0.877
Edema hybrid——overall radio	0.843	0.336
Edema hybrid——overall hybrid	0.846	0.338
Tumor DL——tumor radio	0.345	0.442
Tumor DL——tumor hybrid	0.964	0.353
Tumor DL——overall DL	0.706	0.611
Tumor DL——overall radio	0.835	0.706
Tumor DL——overall hybrid	0.873	0.48
Tumor radio——tumor hybrid	0.365	0.157
Tumor radio——overall DL	0.241	0.32
Tumor radio——overall radio	0.506	0.177
Tumor radio——overall hybrid	0.288	0.081
Tumor hybrid——overall DL	0.725	0.632
Tumor hybrid ——overall radio	0.863	0.911
Tumor hybrid ——overall hybrid	0.848	0.91
Overall DL——overall radio	0.676	0.857
Overall DL——overall hybrid	0.931	0.6
Overall radio——overall hybrid	0.726	0.333

DL, deep learning.
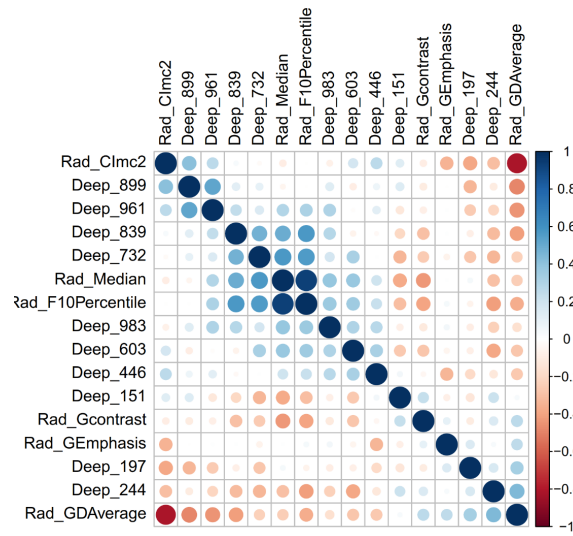
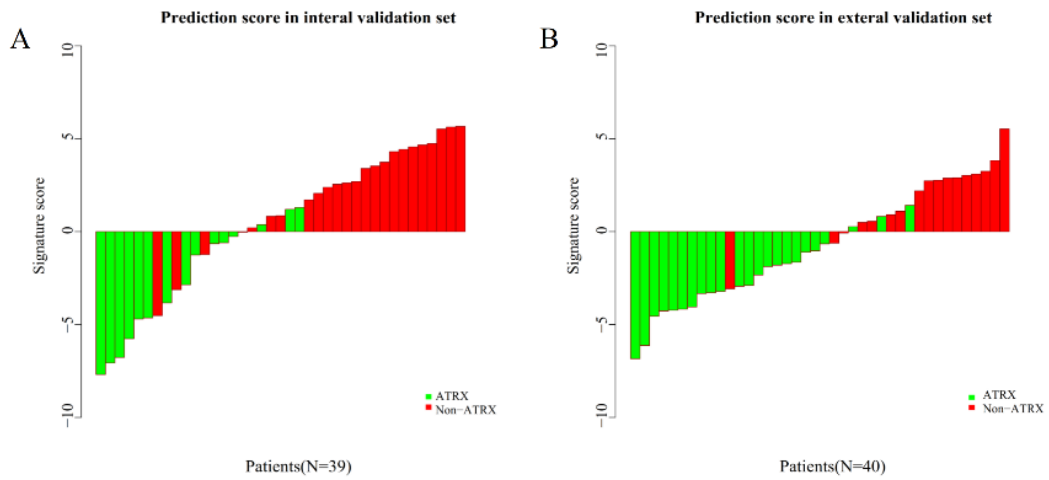**Figure S1** The feature correlation coefficient analysis.

Figure S2 The feature correlation coefficient analysis. (A) Overall hybrid model classification performance on the validation set; (B) overall hybrid model classification performance on the test set.

Appendix 1 Image preprocessing

First, we rigidly aligned each T1c volume to T2f using advanced normalization tools (ANTs). In order to eliminate the difference in brightness on MR images caused by factors such as the scanner itself and many unknown problems, N4 bias field correction was performed using SimpleITK. This employs a hybrid white stripe [22] approach for intensity normalization and uses the ANTs and White Stripe packages in R to complete a statistically principled process of image normalization that preserves intertissue grade and matches the intensity of the tissue without disrupting the natural balance of tissue intensities [23]. At last, isotropic resolution is resampled by using a linear interpolator to reinterpolate all images to 1 mm ×1 mm ×1 mm pixel in the normalized axes.

For the specific formula of radiomics characteristics, see the official Pyradiomics website (https://pyradiomics.readthedocs.io/en/latest). The feature calculation method was used to extract first-order statistics, shape and size, texture, and other features. The specific calculation formulae are listed below follows:

First-order statistics features

First-order statistics features describe the gray-level distribution of all voxels within the ROI.

Let X be a set of all voxels included in the ROI, Np the number of voxels in X, P(i) the first-order histogram with Ng discrete intensity levels, p(i) the normalized first-order histogram equal to P(i)/Np, and c the optional value, which shifts the intensities to prevent negative values in X.

1. Energy

$$energy = \sum_{i=1}^{N_p} (\mathbf{X}(i) + c)^2$$

2. Total energy

$$totalenergy = V_{voxel} \sum_{i=1}^{N_p} (\mathbf{X}(i) + c)^2$$

3. Entropy

$$entropy = -\sum_{i=1}^{N_g} p(i) \log_2 \left(p(i) + \epsilon \right)$$

ϵ is an arbitrarily small positive number ($\approx 2.2 \times 10^{-16}$)

4. Minimum

$$minimum = \min(\mathbf{X})$$

5. 10th percentile

The 10th percentile of X

6. 90th percentile

The 90th percentile of X

7. Maximum

$$maximum = \max(\mathbf{X})$$

8. Mean

$$mean = \frac{1}{N_p} \sum_{i=1}^{N_p} \mathbf{X}(i)$$

9. Median

The median gray-level intensity within the ROI.

10. Interquartile range

$$interquartilerange = \mathbf{P}_{75} - \mathbf{P}_{25}$$

11. Range

$$range = \max(\mathbf{X}) - \min(\mathbf{X})$$

12. Mean absolute deviation

$$MAD = \frac{1}{N_p} \sum_{i=1}^{N_p} | \mathbf{X}(i) - \bar{X} |$$

13. Robust mean absolute deviation (rMAD)

$$rMAD = \frac{1}{N_{10-90}} \sum_{i=1}^{N_{10-90}} | \mathbf{X}_{10-90}(i) - \bar{X}_{10-90} |$$

14. Root mean squared (RMS)

$$RMS = \sqrt{\frac{1}{N_p} \sum_{i=1}^{N_p} (\mathbf{X}(i) + c)^2}$$

15. Skewness

$$skewness = \frac{\mu_3}{\sigma^3} = \frac{\frac{1}{N_p} \sum_{i=1}^{N_p} (\mathbf{X}(i) - \bar{X})^3}{\left(\sqrt{\frac{1}{N_p} \sum_{i=1}^{N_p} (\mathbf{X}(i) - \bar{X})^2} \right)^3}$$

16. Kurtosis

$$kurtosis = \frac{\mu_4}{\sigma^4} = \frac{\frac{1}{N_p} \sum_{i=1}^{N_p} (\mathbf{X}(i) - \bar{X})^4}{\left(\frac{1}{N_p} \sum_{i=1}^{N_p} (\mathbf{X}(i) - \bar{X})^2 \right)^2}$$

17. Variance

$$variance = \frac{1}{N_p} \sum_{i=1}^{N_p} (\mathbf{X}(i) - \bar{X})^2$$

18. Uniformity

$$uniformity = \sum_{i=1}^{N_g} p(i)^2$$

Shape and size features:

This group of features describe the 3-dimensional size and shape of the ROI. Features were derived from a triangle mesh generated using a marching cubes algorithm based on the ROI.

Let Nv be the number of voxels included in the ROI, Nf the number of faces defining the Mesh, V the volume of the mesh in millimeters cubed, and A the surface area of the mesh in millimeters squared.

1. Mesh volume

$$V_i = \frac{Oa_i \cdot (Ob_i \times Oc_i)}{6}$$

$$V = \sum_{i=1}^{N_f} V_i$$

2. Voxel volume

$$V_{voxel} = \sum_{k=1}^{N_v} V_k$$

3. Surface area

$$A_i = \frac{1}{2} |\, \mathbf{a}_i \mathbf{b}_i \times \mathbf{a}_i \mathbf{c}_i \,|$$

$$A = \sum_{i=1}^{N_f} A_i$$

4. Surface area to volume ratio

$$surfacetovolumeratio = \frac{A}{V}$$

5. Sphericity

$$sphericity = \frac{\sqrt[3]{36\pi V^2}}{A}$$

6. Maximum 3D diameter

  Maximum 3D diameter is defined as the largest pairwise Euclidean distance between the tumor surface mesh vertices.

7. Maximum 2D diameter (slice)

  Maximum 2D diameter (slice) is defined as the largest pairwise Euclidean distance between tumor surface mesh vertices in the row–column (generally the axial) plane.

8. Maximum 2D diameter (column)

  Maximum 2D diameter (column) is defined as the largest pairwise Euclidean distance between tumor surface mesh vertices in the row–slice (usually the coronal) plane.

9. Maximum 2D diameter (row)

  Maximum 2D diameter (row) is defined as the largest pairwise Euclidean distance between tumor surface mesh vertices in the column–slice (usually the sagittal) plane.

10. Major axis length

$$majoraxis = 4\sqrt{\lambda_{major}}$$

11. Minor axis length

$$minoraxis = 4\sqrt{\lambda_{minor}}$$

12. Least axis length

$$leastaxis = 4\sqrt{\lambda_{least}}$$

13. Elongation

$$elongation = \sqrt{\frac{\lambda_{minor}}{\lambda_{major}}}$$

14. Flatness

$$flatness = \sqrt{\frac{\lambda_{least}}{\lambda_{major}}}$$

Textural features

Textural features reflect information about the spatial arrangement of voxel intensities and therefore could describe the homogeneity of the ROI. In our study, textural features were derived from 4 statistical feature matrices: 22 from the gray-level co-occurrence matrix (GLCM), 16 from the gray-level run-length texture matrix (GLRLM), 16 from the gray-level size zone matrix (GLSZM), 14 from the gray-level dependence matrix (GLDM), and 5 from neighboring gray-scale difference matrix (NGTDM).

Gray-level co-occurrence matrix (GLCM)

1. Autocorrelation

$$autocorrelation = \sum_{i=1}^{N_g} \sum_{j=1}^{N_g} p(i,j)ij$$

2. Joint average

$$jointaverage = \mu_x = \sum_{i=1}^{N_g} \sum_{j=1}^{N_g} p(i,j)i$$

3. Cluster prominence

$$clusterprominence = \sum_{i=1}^{N_g} \sum_{j=1}^{N_g} \left(i+j-\mu_x-\mu_y\right)^4 p(i,j)$$

4. Cluster shade

$$clustershade = \sum_{i=1}^{N_g} \sum_{j=1}^{N_g} \left(i+j-\mu_x-\mu_y\right)^3 p(i,j)$$

5. Cluster tendency

$$clustertendency = \sum_{i=1}^{N_g} \sum_{j=1}^{N_g} \left(i+j-\mu_x-\mu_y\right)^2 p(i,j)$$

6. Contrast

$$contrast = \sum_{i=1}^{N_g} \sum_{j=1}^{N_g} (i-j)^2 p(i,j)$$

7. Correlation

$$correlation = \frac{\sum_{i=1}^{N_g}\sum_{j=1}^{N_g} p(i,j)ij - \mu_x\mu_y}{\sigma_x(i)\sigma_y(j)}$$

8. Difference average

$$differenceaverage = \sum_{k=0}^{N_g-1} kp_{x-y}(k)$$

9. Difference entropy

$$differenceentropy = \sum_{k=0}^{N_g-1} p_{x-y}(k)\log_2\left(p_{x-y}(k)+\epsilon\right)$$

10. Difference variance

$$differencevariance = \sum_{k=0}^{N_g-1} (k-DA)^2 p_{x-y}(k)$$

11. Joint energy

$$jointenergy = \sum_{i=1}^{N_g} \sum_{j=1}^{N_g} \left(p(i,j)\right)^2$$

12. Joint entropy

$$jointentropy = -\sum_{i=1}^{N_g} \sum_{j=1}^{N_g} p(i,j)\log_2\left(p(i,j)+\epsilon\right)$$

13. Informational measure of correlation (IMC) 1

$$IMC1 = \frac{HXY - HXY1}{\max\{HX,HY\}}$$

14. Informational measure of correlation (IMC) 2

$$IMC2 = \sqrt{1 - e^{-2(HXY2-HXY)}}$$

15. Inverse difference moment (IDM)

$$IDM = \sum_{k=0}^{N_g-1} \frac{p_{x-y}(k)}{1+k^2}$$

16. Inverse difference moment normalized (IDMN)

$$IDMN = \sum_{k=0}^{N_g-1} \frac{p_{x-y}(k)}{1+\left(\dfrac{k^2}{N_g^2}\right)}$$

17. Inverse difference (ID)

$$ID = \sum_{k=0}^{N_g-1} \frac{p_{x-y}(k)}{1+k}$$

18. Inverse difference normalized (IDN)

$$IDN = \sum_{k=0}^{N_g-1} \frac{p_{x-y}(k)}{1+\left(\dfrac{k}{N_g}\right)}$$

19. Inverse variance

$$inversevariance = \sum_{k=1}^{N_g-1} \frac{p_{x-y}(k)}{k^2}$$

20. Maximum probability

$$maximumprobability = \max\left(p(i,j)\right)$$

21. Sum entropy

$$sumentropy = \sum_{k=2}^{2N_g} p_{x+y}(k)\log_2\left(p_{x+y}(k)+\epsilon\right)$$

22. Sum of squares

$$sumsquares = \sum_{i=1}^{N_g} \sum_{j=1}^{N_g} (i-\mu_x)^2 p(i,j)$$

Gray-level run-length texture matrix (GLRLM)

1. Short run emphasis (SRE)

$$SRE = \frac{\sum_{i=1}^{N_g} \sum_{j=1}^{N_r} \dfrac{\mathbf{P}(i,j\mid\theta)}{j^2}}{N_r(\theta)}$$

2. Long run emphasis (LRE)

$$LRE = \frac{\sum_{i=1}^{N_g} \sum_{j=1}^{N_r} \mathbf{P}(i,j\mid\theta)j^2}{N_r(\theta)}$$

3. Gray-level nonuniformity (GLN)

$$GLN = \frac{\sum_{i=1}^{N_g}\left(\sum_{j=1}^{N_r} \mathbf{P}(i,j\mid\theta)\right)^2}{N_r(\theta)}$$

4. Gray-level nonuniformity normalized (GLNN)

$$GLNN = \frac{\sum_{i=1}^{N_g}\left(\sum_{j=1}^{N_r} \mathbf{P}(i,j\mid\theta)\right)^2}{N_r(\theta)^2}$$

5. Run length nonuniformity (RLN)

$$RLN = \frac{\sum_{j=1}^{N_r}\left(\sum_{i=1}^{N_g} \mathbf{P}(i,j\mid\theta)\right)^2}{N_r(\theta)}$$

6. Run length nonuniformity normalized (RLNN)

$$RLNN = \frac{\sum_{j=1}^{N_r}\left(\sum_{i=1}^{N_g} \mathbf{P}(i,j\mid\theta)\right)^2}{N_r(\theta)^2}$$

7. Run percentage (RP)

$$RP = \frac{N_r(\theta)}{N_p}$$

8. Gray-level variance (GLV)

$$GLV = \sum_{i=1}^{N_g} \sum_{j=1}^{N_r} p(i,j\mid\theta)(i-\mu)^2$$

9. Run variance (RV)

$$RV = \sum_{i=1}^{N_g} \sum_{j=1}^{N_r} p(i,j\mid\theta)(j-\mu)^2$$

10. Run entropy (RE)

$$RE = -\sum_{i=1}^{N_g} \sum_{j=1}^{N_r} p(i,j\mid\theta)\log_2(p(i,j\mid\theta)+\epsilon)$$

11. Low gray-level run emphasis (LGLRE)

$$LGLRE = \frac{\sum_{i=1}^{N_g} \sum_{j=1}^{N_r} \dfrac{\mathbf{P}(i,j\mid\theta)}{i^2}}{N_r(\theta)}$$

12. High gray-level run emphasis (HGLRE)

$$HGLRE = \frac{\sum_{i=1}^{N_g} \sum_{j=1}^{N_r} \mathbf{P}(i,j\mid\theta)i^2}{N_r(\theta)}$$

13. Short run low gray-level emphasis (SRLGLE)

$$SRLGLE = \frac{\sum_{i=1}^{N_g} \sum_{j=1}^{N_r} \dfrac{\mathbf{P}(i,j\mid\theta)}{i^2 j^2}}{N_r(\theta)}$$

14. Short run high gray-level emphasis (SRHGLE)

$$SRHGLE = \frac{\sum_{i=1}^{N_g} \sum_{j=1}^{N_r} \dfrac{\mathbf{P}(i,j\mid\theta)i^2}{j^2}}{N_r(\theta)}$$

15. Long run low gray-level emphasis (LRLGLE)

$$LRLGLRE = \frac{\sum_{i=1}^{N_g} \sum_{j=1}^{N_r} \dfrac{\mathbf{P}(i,j\mid\theta)j^2}{i^2}}{N_r(\theta)}$$

16. Long run high gray-level emphasis (LRHGLE)

$$LRHGLRE = \frac{\sum_{i=1}^{N_g} \sum_{j=1}^{N_r} \mathbf{P}(i,j\mid\theta)i^2 j^2}{N_r(\theta)}$$

Gray-level size zone matrix (GLSZM)

1. Small area emphasis (SAE)

$$SAE = \frac{\sum_{i=1}^{N_g} \sum_{j=1}^{N_s} \dfrac{\mathbf{P}(i,j)}{j^2}}{N_z}$$

2. Large area emphasis (LAE)

$$LAE = \frac{\sum_{i=1}^{N_g}\sum_{j=1}^{N_s}\mathbf{P}(i,j)j^2}{N_z}$$

3. Gray-level nonuniformity (GLN)

$$GLN = \frac{\sum_{i=1}^{N_g}\left(\sum_{j=1}^{N_s}\mathbf{P}(i,j)\right)^2}{N_z}$$

4. Gray-level nonuniformity normalized (GLNN)

$$GLNN = \frac{\sum_{i=1}^{N_g}\left(\sum_{j=1}^{N_s}\mathbf{P}(i,j)\right)^2}{N_z^2}$$

5. Size–zone nonuniformity (SZN)

$$SZN = \frac{\sum_{j=1}^{N_s}\left(\sum_{i=1}^{N_g}\mathbf{P}(i,j)\right)^2}{N_z}$$

6. Size–zone nonuniformity normalized (SZNN)

$$SZNN = \frac{\sum_{j=1}^{N_s}\left(\sum_{i=1}^{N_g}\mathbf{P}(i,j)\right)^2}{N_z^2}$$

7. Zone percentage (ZP)

$$ZP = \frac{N_z}{N_p}$$

8. Gray-level variance (GLV)

$$GLV = \sum_{i=1}^{N_g}\sum_{j=1}^{N_s}p(i,j)(i-\mu)^2$$

9. Zone variance (ZV)

$$ZV = \sum_{i=1}^{N_g}\sum_{j=1}^{N_s}p(i,j)(j-\mu)^2$$

10. Zone entropy (ZE)

$$ZE = -\sum_{i=1}^{N_g}\sum_{j=1}^{N_s}p(i,j)\log_2(p(i,j)+\epsilon)$$

11. Low gray-level zone emphasis (LGLZE)

$$LGLZE = \frac{\sum_{i=1}^{N_g}\sum_{j=1}^{N_s}\dfrac{\mathbf{P}(i,j)}{i^2}}{N_z}$$

12. High gray-level zone emphasis (HGLZE)

$$HGLZE = \frac{\sum_{i=1}^{N_g}\sum_{j=1}^{N_s}\mathbf{P}(i,j)i^2}{N_z}$$

13. Small area low gray-level emphasis (SALGLE)

$$SALGLE = \frac{\sum_{i=1}^{N_g}\sum_{j=1}^{N_s}\dfrac{\mathbf{P}(i,j)}{i^2 j^2}}{N_z}$$

14. Small area high gray-level emphasis (SAHGLE)

$$SAHGLE = \frac{\sum_{i=1}^{N_g}\sum_{j=1}^{N_s}\dfrac{\mathbf{P}(i,j)i^2}{j^2}}{N_z}$$

15. Large area low gray-level emphasis (LALGLE)

$$LALGLE = \frac{\sum_{i=1}^{N_g}\sum_{j=1}^{N_s}\dfrac{\mathbf{P}(i,j)j^2}{i^2}}{N_z}$$

16. Large area high gray-level emphasis (LAHGLE)

$$LAHGLE = \frac{\sum_{i=1}^{N_g}\sum_{j=1}^{N_s}\mathbf{P}(i,j)i^2 j^2}{N_z}$$

Gray-level dependence matrix (GLDM)

1. Small dependence emphasis (SDE)

$$SDE = \frac{\sum_{i=1}^{N_g}\sum_{j=1}^{N_d}\dfrac{\mathbf{P}(i,j)}{i^2}}{N_z}$$

2. Large dependence emphasis (LDE)

$$LDE = \frac{\sum_{i=1}^{N_g}\sum_{j=1}^{N_d}\mathbf{P}(i,j)j^2}{N_z}$$

3. Gray-level nonuniformity (GLN)

$$GLN = \frac{\sum_{i=1}^{N_g} \left(\sum_{j=1}^{N_d} \mathbf{P}(i,j) \right)^2}{N_z}$$

4. Dependence nonuniformity (DN)

$$DN = \frac{\sum_{j=1}^{N_d} \left(\sum_{i=1}^{N_g} \mathbf{P}(i,j) \right)^2}{N_z}$$

5. Dependence nonuniformity normalized (DNN)

$$DNN = \frac{\sum_{j=1}^{N_d} \left(\sum_{i=1}^{N_g} \mathbf{P}(i,j) \right)^2}{N_z^2}$$

6. Gray-level variance (GLV)

$$GLV = \sum_{i=1}^{N_g} \sum_{j=1}^{N_d} p(i,j)(i-\mu)^2, \text{where} \mu = \sum_{i=1}^{N_g} \sum_{j=1}^{N_d} ip(i,j)$$

7. Dependence variance (DV)

$$DV = \sum_{i=1}^{N_g} \sum_{j=1}^{N_d} p(i,j)(j-\mu)^2, \text{where} \mu = \sum_{i=1}^{N_g} \sum_{j=1}^{N_d} jp(i,j)$$

8. Dependence entropy (DE)

$$DependenceEntropy = -\sum_{i=1}^{N_g} \sum_{j=1}^{N_d} p(i,j)\log_2(p(i,j)+\epsilon)$$

9. Low gray-level emphasis (LGLE)

$$LGLE = \frac{\sum_{i=1}^{N_g} \sum_{j=1}^{N_d} \frac{\mathbf{P}(i,j)}{i^2}}{N_z}$$

10. High gray-level emphasis (HGLE)

$$HGLE = \frac{\sum_{i=1}^{N_g} \sum_{j=1}^{N_d} \mathbf{P}(i,j)i^2}{N_z}$$

11. Small dependence low gray-level emphasis (SDLGLE)

$$SDLGLE = \frac{\sum_{i=1}^{N_g} \sum_{j=1}^{N_d} \frac{\mathbf{P}(i,j)}{i^2 j^2}}{N_z}$$

12. Small dependence high gray-level emphasis (SDHGLE)

Measures the joint distribution of small dependence with higher gray-level values.

13. Large dependence low gray-level emphasis (LDLGLE)

$$LDLGLE = \frac{\sum_{i=1}^{N_g} \sum_{j=1}^{N_d} \frac{\mathbf{P}(i,j) j^2}{i^2}}{N_z}$$

14. Large dependence high gray-level emphasis (LDHGLE)

$$LDHGLE = \frac{\sum_{i=1}^{N_g} \sum_{j=1}^{N_d} \mathbf{P}(i,j) i^2 j^2}{N_z}$$

Neighboring gray-scale difference matrix (NGTDM)

1. Coarseness

$$Coarseness = \frac{1}{\sum_{i=1}^{N_g} p_i s_i}$$

2. Contrast

$$Contrast = \left(\frac{1}{N_{g,p}(N_{g,p}-1)} \sum_{i=1}^{N_g} \sum_{j=1}^{N_g} p_i p_j (i-j)^2 \right) \left(\frac{1}{N_{v,p}} \sum_{i=1}^{N_g} s_i \right), \text{where } p_i \neq 0, p_j \neq 0$$

3. Busyness

$$Busyness = \frac{\sum_{i=1}^{N_g} p_i s_i}{\sum_{i=1}^{N_g} \sum_{j=1}^{N_g} |i p_i - j p_j|}, \text{where } p_i \neq 0, p_j \neq 0$$

4. Complexity

$$Complexity = \frac{1}{N_{v,p}} \sum_{i=1}^{N_g} \sum_{j=1}^{N_g} |i-j| \frac{p_i s_i + p_j s_j}{p_i + p_j}, \text{where } p_i \neq 0, p_j \neq 0$$

5. Strength

$$Strength = \frac{\sum_{i=1}^{N_g} \sum_{j=1}^{N_g} (p_i + p_j)(i-j)^2}{\sum_{i=1}^{N_g} s_i}, \text{where } p_i \neq 0, p_j \neq 0$$

Features extracted from wavelet-filtered images

After wavelet decomposition, low-level information hidden from the human eye can be exposed. In our study, Coiflet 1 wavelet was used to decompose the original image. High- and low-pass filters were applied stepwise on the x, y, and z coordinates, which generated 8 decompositions from 1 patient's image. The 14 first-order statistics and 68 textural features described above were extracted from all of 8 decompositions. Thus, a total of 728 wavelet features were extracted from each sequence.

Features extracted from Laplacian of Gaussian–filtered images

Application of a Laplacian of Gaussian filter to the input image yields a derived image for each Σ value specified. A Laplacian of Gaussian image is obtained by convolving the image with the second derivative (Laplacian) of a Gaussian kernel. The Gaussian kernel is used to smooth the image and is defined as follows:

$$G(x,y,z,\sigma) = \frac{1}{(\sigma\sqrt{2\pi})^3} e^{-\frac{x^2+y^2+z^2}{2\sigma^2}}$$

The Gaussian kernel is convolved with the Laplacian kernel $\nabla 2G(x,y,z)$, which is sensitive to areas with rapidly changing intensities, enhancing edges. The width of the filter in the Gaussian kernel is determined by σ and can be used to emphasize more fine (low σ values) or coarse (high σ values) textures.

Appendix 2 The formula for imaging score of imaging signature

Imaging Score =DL_t1c_197 × (0.874) + DL_t2f_603 × 0.776 + DL_t2f_732 × 0.248 + DL_t2f_899 × 1.089+DL_t2f_961 × 0.791+DL_t1c_151 × (–0.633) + DL_t1c_446 × 0.1 + Radio_t1c_GLCM_Contrast × (–0.847) + Radio_t2f_GLSZM_Emphasis × (–0.8108) + DL_t2f_839 × 0.476 + DL_t2f_244 × (–0.256) + DL_t2f_983 × 0.746 + DL_t2f_Firstorder_Median × 0.440+Radio_t2f_GLCM_Imc2 × 0.976 + Radio_t2f_Firstorder_10Percentile × 1.17 + Radio_t2f_GLCM Average × 0.5937
(DL, deep learning; t2f, T2 fluid-attenuated inversion recovery; T1c, contrast-enhanced T1-weighted; GLCM, gray-level co-occurrence matrix; GLSZM, gray-level size zone matrix)